LUND
UNIVERSITY

A Thesis submitted for the degree of Master of Science

Project Duration: 60hp

Nuclear Structure near the Proton Drip Line: A Search for Excited States in ^{62}Ge

---

Author:
Dalia Farghaly

Supervisor:
Professor Dirk Rudolph
Co-supervisor:
Doctoral Candidate Yuliia Hrabar

Department of Physics

Division of Nuclear Physics

March 2022

Abstract

An experiment to study mirror symmetry in the mass $A = 60$ region was performed at the Argonne National Laboratory (ANL) in 2020. The fusion-evaporation reaction ^{40}Ca + ^{24}Mg $\rightarrow$ ^{64}Ge* at a beam energy of 106 MeV was used to populate excited states in ^{62}Ge. The experimental setup used was made up of various detector systems, including Gammasphere for γ-ray detection, Microball in combination with two CD-type Double Sided Strip Detectors to measure evaporated charged particles, the Neutron Shell to observe evaporated neutrons, and the Fragment Mass Analyser with the Ionisation Chamber, to determine the mass and charge of reaction products. Energy and efficiency calibrations of Gammasphere were carried out as part of data processing in this thesis work. Microball and Silicon detectors were used to perform anti-coincidence, and the Neutron Shell detector data was processed to highlight the two-neutron evaporation channel of ^{62}Ge. An alternative attempt to select nuclei of $A = 62$ using the Fragment Mass Analyser in combination with the Ionisation Chamber was made. A calibration of the Ionisation Chamber was carried out as well as one optimisation of the Z resolution by combining energy loss signals in each part of the chamber to construct energy-loss functions. At the present stage of analysis of this dataset, there is no conclusive evidence confirming any transitions in ^{62}Ge.

Acknowledgments

First and foremost, I would like to thank my main supervisor, Professor Dirk Rudolph. Thank you for sparking my interest in the field of nuclear physics years ago as a bachelor student and inspiring me in so many ways. I am so thankful for the hours we spent looking at spectra together and all the support and expert guidance, without which this project would not have been possible. You are an example of an ideal supervisor, and someone I will always look up to. To my co-supervisor, Yuliia Hrabar, I want to thank you for your infinite patience with me, and always taking the time to explain things clearly and pedagogically. Thank you for teaching me how to meet challenges head on, one after the other. I feel privileged to have had such amazing and dedicated supervisors. I am also grateful for all the time I was able to spend with the Nuclear Structure Group, which was a big part of my life in Lund, and sharing different ideas and laughs over lunch and coffee breaks. Lastly, I would like to thank my mother, Elizabeth, and all my friends for their support and love during this time.

Contents

1 Introduction **1**

2 Fundamentals of Detection **4**
1 Principles of γ-ray Detection 4
1.1 Working of a HPGe Detector 6
1.2 Anti-Compton Shielding 6
2 Principles of Charged-Particle Detection 7
3 Principles of Neutron Detection 7

3 Experimental Campaign **8**
1 Fusion-Evaporation Reactions 8
2 Experimental Setup 10
2.1 Gammasphere 11
2.2 Microball + Si Detectors 12
2.3 Neutron Shell 13
2.4 Fragment Mass Analyser 13
2.5 Ionisation Chamber 14

4 Data Handling **15**
1 Analysis Methods 16
2 Gammasphere: Data Preparation 17
2.1 Doppler Correction 17
2.2 Energy Calibration 17
2.3 Efficiency Calibration 19
3 Reaction Channel Selection 20
3.1 Charged Particle Discrimination 20
3.2 Neutron Discrimination 21
3.3 Missing Neutrons 23
4 Mass Selection 24
4.1 A/Q 24
4.2 Optimising Mass Selection 24
4.3 Timing Coincidences 24
5 Ionisation Chamber: Data Preparation 26
5.1 Recoil Proton Number Selection 26
5.2 Energy-Loss Functions 26

5.3 Optimising Z Separation 28

5 Results and Discussion **29**
1 The Recoil-γ Matrix 29
2 Selecting the ELF 30
3 Gated Spectra 31
3.1 $A = 61$ Separation 31
3.2 $A = 62$ Separation 33
4 Investigating Tentative ^{62}Ge Transitions 34

6 Conclusions and Outlook **35**
A Appendix 37

List of Figures

1.1 Excerpt from the nuclidic chart around the $A = 60$ region 2

2.1 Relative cross-section of different modes of interaction with respect to photon energy in Ge detectors 4

3.1 De-excitation of a nucleus with respect to the yrast line 9
3.2 Main reaction channels 9
3.3 Schematic diagram of the complete experimental setup 10
3.4 A schematic drawing showing the side-view design of GAMMASPHERE 11
3.5 Photographs of MICROBALL and DSSD 12
3.6 Schematic diagram of the FMA 13

4.1 Flow chart illustrating two possible analysis methods 16
4.2 HPGe detetor alignment 18
4.3 Energy source calibration line 18
4.4 Efficiency calibration curve 19
4.5 Proton and α gates on MICROBALL spectra 20
4.6 Neutron gates on Neutron Shell spectra 22
4.7 Control spectra to verify quality of neutron gates 22
4.8 Comparison of WUDAQ and FMA event rate 23
4.9 A/Q plot agreement with detected recoils. 25
4.10 Uncorrected Ionisation Chamber spectra 27
4.11 Corrected Ionisation Chamber spectra 28

5.1 Recoil-γ matrix showing distribution of peaks in ^{62}Zn and ^{62}Ga nuclei. . . . 29
5.2 IC spectra comparing effect of straightening iterations 30
5.3 IC spectra for^{61}Zn and ^{61}Cu 31
5.4 ^{61}Zn and ^{61}Cu spectra overlaid 32
5.5 Cleaned ^{61}Zn γ spectrum 32
5.6 IC spectra for^{61}Zn and ^{61}Cu 33
5.7 Background subtracted IC spectrum for ^{62}Ga 34

List of Abbreviations

ACS: Anti-Compton Shield
ANL: Argonne National Laboratory
ATLAS: Argonne Tandem Linac Accelerator System
BGO: Bismuth Germanate ($Bi_4Ge_3O_{12}$)
CsI(Tl): Caesium Iodide-Thallium activated
DAQ: Data Acquisition System
DFMA: Digital Fragment Mass Analyser
DGS: Digital GAMMASPHERE
DSSD: Double-Sided Silicon-strip Detector
ELF: Energy-Loss Function
FMA: Fragment Mass Analyser
FWHM: Full Width Half Maximum
HPGe: High-Purity Germanium
IC: Ionisation Chamber
PD: PhotoDiode
PMT: PhotoMultiplier Tube
PPAC: Parallel Plate Avalanche Counter
PSD: Pulse Shape Discrimination
TOF: Time Of Flight
WUDAQ: Washington University Data Acquisition System

Chapter 1

Introduction

The atomic nucleus is a many-body quantum mechanical system composed of strongly interacting fermions, protons and neutrons. It displays many interesting characteristics and phenomena which are studied in contemporary nuclear physics. All existing nuclei can be characterized and placed on the nuclidic chart by plotting their proton numbers versus their neutron numbers, denoted by Z and N, respectively. Lighter nuclei containing equal numbers of protons and neutrons ($N \simeq Z$) follow the line of stability. At this line of stability, nuclei have the highest binding energies, and hence are the most stable. As one moves away from this line, the nuclei begin to have more extreme proton-to-neutron ratios and become increasingly unstable. They decay towards the line of stability. The boundaries of this region, often referred to as "the valley of stability", are marked by the proton and neutron drip lines. No stable atomic nuclei exist beyond the proton and neutron drip lines, after which the nuclei will decay via the emission of one or more protons or neutrons.

During the late 1940s, the nuclear shell model was developed. It is a model based on the Pauli exclusion principle, which dictates that no two fermions can occupy the same quantum state. It was empirically discovered that some nuclei with particular numbers of protons and neutrons were more tightly bound than their adjacent neighbouring nuclei. This led to the discovery of "magic numbers", which motivated scientists to propose the existence of a shell structure in the nucleus, where every nucleon occupies a defined quantum state. A mean-field approach suggests that the nucleons move in an effective potential well and experience an average force due to all the other nucleons. Modelling these potential wells accurately is necessary for determining the energy levels within the shell model. Significant theoretical efforts are being made to accurately construct them. The construction of the nuclear shells depends on the type of potential modelled. Some low lying energy levels in a single-particle shell model, constructed using a harmonic oscillator potential are: $1s, 1p, 1d, 2s, 1f, 2p$. The levels split up further due to a spin-orbit interaction term introduced on the level of the nuclear force. Studying shell structure of exotic nuclei situated far from the line of stability is vital to understanding the mean-field model of the nucleus, because it can offer insights to the limits of theoretical shell-model descriptions and provide some understanding of how the nuclear strong force varies with proton-to-neutron ratios.

γ-ray spectroscopy is a technique employed in order to study nuclear systems in extreme conditions, for example, high temperatures and angular momenta, by analysing the energy spectra of γ rays emitted from excited states in nuclei. This thesis work concentrates on the region just above the doubly-magic nucleus ^{56}Ni, where the particle-unbound states hit both the $N = Z$ line, and the astrophysical rapid capture (rp) process begins. The data set analysed in this thesis was taken during a campaign at the Argonne National Laboratory (ANL) [1], Chicago, USA, in the summer of 2020. Two CD-type double sided Si-strip detectors (DSSDs) [2] were used in combination with MICROBALL [3], GAMMASPHERE [4], Neutron Shell [5], and the Fragment Mass Analyser (FMA) [6], to perform high resolution particle- and γ-ray coincidence spectroscopy.

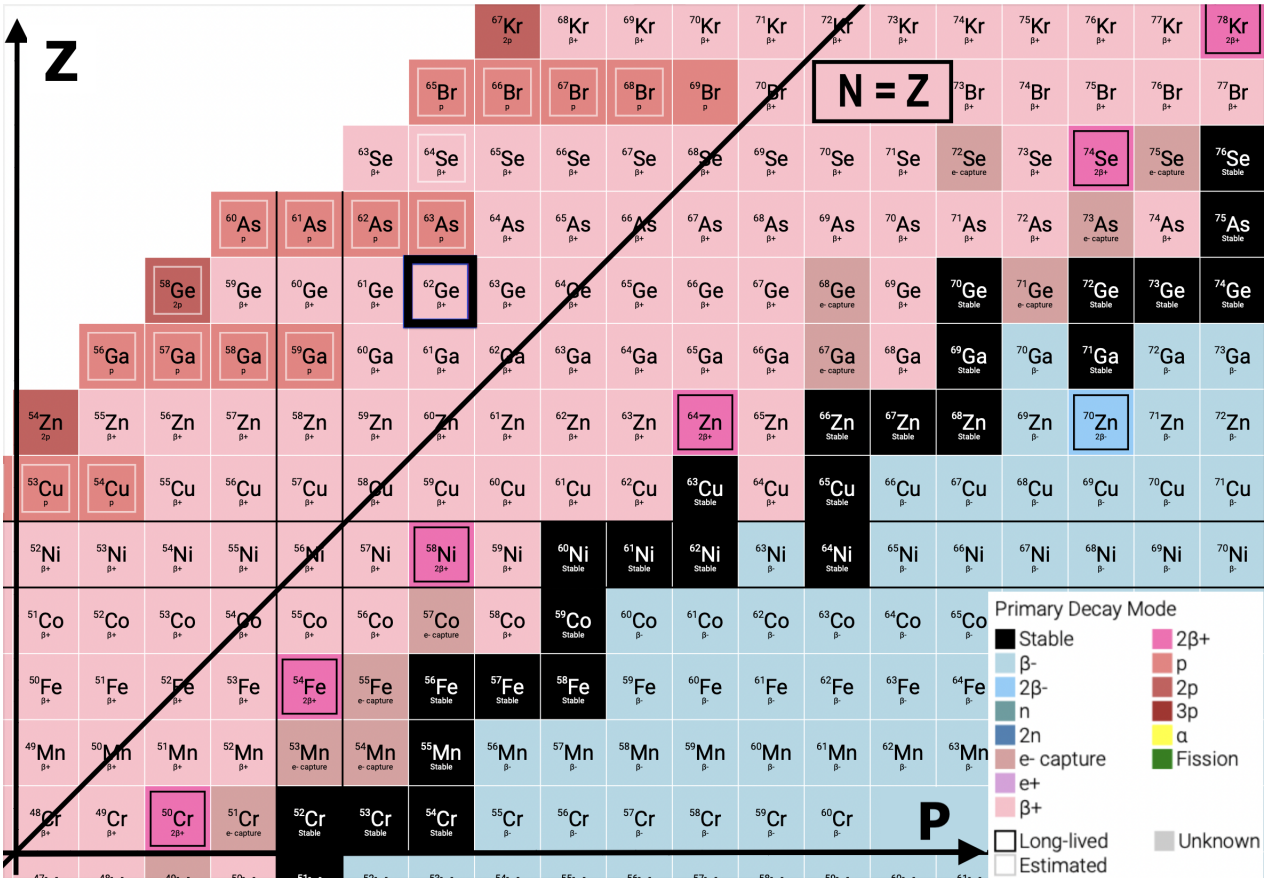

Figure 1.1: Excerpt from the nuclidic chart around the $A = 60$ region with the $N = Z$ line marked. Atomic nuclei on the line of stability are shown in black. ^{62}Ge, which lies above the doubly magic nucleus ^{56}Ni, is outlined [7].

Mirror nuclei, which are of interest in this thesis, are nuclei where the proton and neutron numbers are mutually interchanged. They have similar binding energies since the strong force is invariant with respect to proton and neutron number. This means that the electromagnetic force (Coulomb interaction) is the major force affecting the discrepancy in energy levels between mirror nuclei. The Coulomb force only depends on the spatial arrangement of the

protons within the nucleus and its shape, which in turn depends on its energy and angular momentum. Investigating this mirror symmetry in nuclei in the $A = 60$ region can offer a deeper understanding of interactions within the nucleus, and can be a good benchmark to test the accuracy of current theoretical descriptions.

The reaction of interest is ^{40}Ca + ^{24}Mg $\rightarrow$ ^{64}Ge*. ^{62}Ge, about which little is known to date [8] [9] [10], is the relevant nucleus in this thesis. It is produced in the two-neutron ($2n$) evaporation channel. Identifying and classifying its excited states in the $A = 60$ region, as seen in Figure 1.1, will offer more insight into processes like isospin symmetry breaking in mirror systems beyond ^{56}Ni and the rp-capture process. Isospin symmetry, a fundamental symmetry in nuclei is broken due to the Coulomb interactions and small differences in interaction strengths of proton-proton, neutron-proton, and neutron-neutron, which in turn could be caused by mass differences in the up and down quarks and the electromagnetic interaction between them. This difference in interaction strengths can be studied by investigating different isospin-symmetry phenomena, such as the Mirror Energy Difference (MED) [11]. The rp-process in which nuclei accumulate protons, and is significant in the nucleosynthesis of heavier nuclei. It occurs on the proton rich side of the nuclidic chart, close to the proton drip-line (as seen in Figure 1.1), and the exact termination point is not yet well established due to a lack of knowledge of nuclear properties of nuclei near the proton dripline [12]. The aim of this work is to confirm and extend the decay scheme of the exotic nucleus ^{62}Ge, and compare its level structure to its mirror nucleus ^{62}Zn - allowing a more detailed study of mirror symmetry in the upper *fp* shell [2].

Chapter 2

Fundamentals of Detection

The experimental setup concerned in this thesis consists of many different types of detector arrays used to detect different types of ionizing radiation. These include electromagnetic radiation such as γ rays and x rays, charged particles such as α particles and protons, as well as neutrons. This chapter aims to give a brief reminder of how these different kinds of radiation interact with matter and what kind of technology is used to detect them in the setup exploited in this thesis.

1 Principles of γ-ray Detection

When a photon meets matter, it can interact in three major ways: photoelectric absorption, Compton scattering, and pair production. In this experiment, GAMMASPHERE, a germanium based detector (described in detail in Chapter 3, Section 2.1) is used to detect the emitted γ rays. The relative probability of possible interactions in germanium with respect to the energy of the γ rays is shown in Figure 2.1, where Compton scattering and the photoelectric effect are the dominant modes of interaction in the energy range of interest (50 keV to 2 MeV).

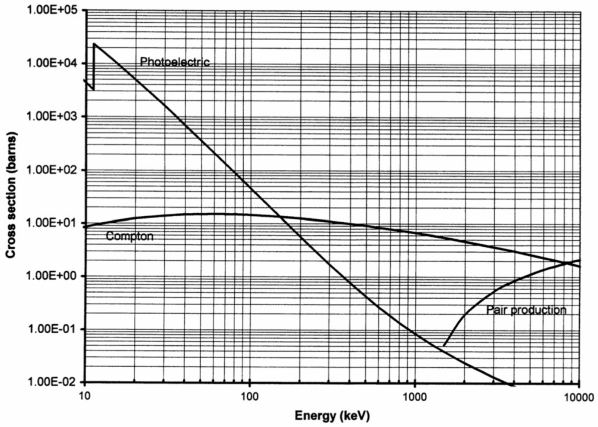

Figure 2.1: Relative cross-section of different modes of interaction with respect to γ-ray energy in Ge detectors [13].

Pair Production

Pair production becomes the most dominant mode of interaction for γ rays with energies $\geq$5 MeV. At high energies like this, the γ ray energy may be converted to mass and can give rise to a particle and its antiparticle. However, we will not be dealing with γ rays of such high energy in this thesis.

Photoelectric Absorption

The photoelectric effect happens when an incoming photon, in this case γ ray, is completely absorbed by an atom, after which an energetic photo-electron is ejected from a bound shell. The γ ray transfers the required energy to free the electron, and the remaining γ-ray energy is contained in the kinetic energy of the now free electron.

Compton Scattering

Compton scattering is a phenomenon which occurs when a γ ray scatters with an outer-shell electron and transfers a part of its energy to the electron. The scattered γ ray which will continue to travel through the medium at angle θ with a lower energy, may Compton scatter multiple times, and finally interact by photoelectric absorption. Equation 2.1 describes the reduced photon energy after scattering (E'_γ), where E_γ is the energy and α is the ratio between the energy of the photon and the electron rest energy, $\alpha = E_\gamma/mc^2$.

$$E'_\gamma = \frac{E_\gamma}{1 + \alpha(1 - cos\theta)} \tag{2.1}$$

The probability of a photon Compton scattering is dependent on its incident energy, as seen in Figure 2.1. One can calculate the probability of an unpolarised photon Compton scattering using the Klein-Nishina formula, where θ is the scattering angle, r_0 is the electronic radius.

$$\frac{d\theta}{d\Omega} = r_0^2\Big[\frac{1}{1 + a(1 - cos\theta)}\Big]^3\Big[\frac{1 + cos\theta}{2}\Big]\Big[1 + \frac{\alpha^2(1 - cos\theta)^2}{(1 + cos\theta)[1 + \alpha(1 - cos\theta)]}\Big] \tag{2.2}$$

It is then possible to calculate the absorption of photons, by integrating the Klein-Nishina formula, as seen in equation 2.3 below.

$$\sigma = \frac{\pi {r_0}^2}{\alpha}\left\{\Big[1 - \frac{2(\alpha + 1)}{\alpha^2}\Big]\ln(2\alpha + 1) + \frac{1}{2} + \frac{4}{\alpha} - \frac{1}{2(2\alpha + 1)^2}\right\} \tag{2.3}$$

Because of the fact that the photons do not scatter discretely in the Ge detectors, one observes a Compton continuum. Consequently, this raises the sensitivity limit for low intensity lines. Since some of the reaction channels produced in this experiment, such as the $2n$ evaporation channel investigated in this thesis, are relatively weak, it can be challenging to distinguish them from background. Anti-Compton Shielding (ACS) is a widely used method to counteract this effect and provide spectra with a better signal-to-noise ratio. More details on this can be found in Section 1.2.

1.1 Working of a HPGe Detector

High Purity Germanium (HPGe) detectors are semi-conductor detectors that are very suitable for performing precise γ-ray and x-ray spectroscopy. This is because Ge has a reasonably high atomic number and a large linear attenuation coefficient leading to a shorter mean-free-path. Typically, a p-doped material is placed in contact with an n-doped material, creating a "depletion zone". The size of the depletion zone can be extended and controlled by applying a bias across the detector medium. There is a lack of charge carriers and an electric field is present across this zone, such that electron and electron-hole pairs can be created by ionising radiation. The average energy required to create an electron-hole pair is 2.9 eV. Ge detectors can also have a depletion zone spanning over several centimetres, making it possible to completely absorb photons of energies up to a few MeV [14]. However, because Ge has a band gap of around 1 eV, electrons can be thermally excited and jump the band gap at room temperature. For this reason, the HPGe crystals have to be cooled down to ≈ 190°C to prevent thermal excitation of electrons across the conduction band. This is typically done through the use of liquid nitrogen dewars, however some more modern HPGe detector systems are electronically cooled. When γ rays enter the depletion zone, they ionise the the material by kicking out an outer shell electron according to the processes above. Along their slowing-down path, these electrons create electron and electron-hole pairs. The number of electron-hole pairs created is proportional to the energy of the secondary electrons. The charges will begin to migrate across the electric field and produce a signal which can be read out by the front-end electronics. The signal is digitised and recorded by the data acquisition system.

1.2 Anti-Compton Shielding

Important parameters to consider when working with HPGe detectors are the energy resolution, sensitivity, and efficiency. The latter is dependent on the peak-to-total ratio, which is defined as the ratio between the number of counts in each photopeak and the total number of events in the spectrum. Because γ rays can Compton scatter outside of the HPGe crystal, it is important to keep track of them since they will not contribute statistically to the full-energy peak, thereby affecting the peak-to-total ratio. This can be done by using Compton suppression. Compton suppression is a technique in which the HPGe is surrounded by an anti-compton shield typically made of Bismuth-Germanate (BGO). The BGO shield essentially acts as a scintillator detector. By implementing a time-coincidence of a γ ray signal detected in the BGO and in the HPGe crystal, it is possible to veto the event and exclude it from further analysis. GAMMASPHERE is made up of several modules, each containing its own ACS. See Figure 3.4 for more details. BGO is the material typically selected for this purpose because it offers good timing properties and a high γ ray detection efficiency, which is useful when performing such anti-coincidence measurements. It also has a density of 7.1 g/cm^2 which guarantees that the scattered γ rays will interact and eventually be stopped in the shield, not travelling to adjacent HPGe crystals. The use of a high-density material also allows the shielding to be thinner. Thus, less solid angle is lost when the detectors are placed into an array. More information on array-like detectors such as GAMMASPHERE, can be found in Section 2.1.

2 Principles of Charged-Particle Detection

Charged particles can be detected with different types of technologies. These include semiconductor detectors which work based on the same principle described in Section 1.1, as well as scintillator detectors. Scintillators are made of luminescent materials which absorb incoming radiation and re-emit it in the form of optical light. This can then be collected by either a photodiode (PD) or a photocathode, followed by a photomultiplier tube (PMT). In both cases, an electrical signal is produced, proportional to the incoming particle's energy. The aim is to stop the incoming particles fully such that the full energy can be reconstructed and particle identification plots can be produced. The stopping power of a material can be calculated using the Bethe-Bloch formula as seen in Eq 2.4, where $\beta = v/c$, v is the particle velocity, c is the speed of light, z is the particle's proton number, E is the particle's energy, x is the distance the particle traverses, n is the electron number density of the medium, I is the mean excitation potential, ϵ_0 is the vacuum permittivity, e is the electron charge, and m_e is the mass of an electron.

$$-\left\langle \frac{dE}{dx} \right\rangle = \frac{4\pi}{m_e} \cdot \frac{nz^2}{\beta^2} \cdot \left(\frac{e^2}{4\pi\epsilon_0}\right)^2 \cdot \left[\ln\left(\frac{2m_e c^2\beta^2}{I \cdot (1-\beta^2)}\right) - \beta^2\right] \tag{2.4}$$

The detection of charged particles (mainly protons and α particles) in this experiment is done with the help of the MICROBALL [3]. The setup contains both silicon detectors (CD-DSSDs) and scintillator detectors (CsI detectors). The DSSDs are pixelated to allow position sensitive measurement of incoming charged particles. More information on MICROBALL can be found in Chapter 3, Section 2.2.

3 Principles of Neutron Detection

Neutrons can be more challenging to detect because they do not have electrical charge. This means that they cannot directly ionise the detector medium. Therefore, the detectors must rely upon a conversion process where the incident neutron interacts with nuclei in the detector to produce a charged particle. This secondary charged particle can then be detected and the interaction of the neutron can be deduced. Hydrogen-rich materials have a high cross-section for interaction with neutrons, and therefore make good candidates when deciding on a detector material to use. Detection of neutrons in this experiment was done by the Neutron Shell [5], a modular neutron detector using liquid scintillators. More details about the Neutron Shell can be found in Chapter 3 Section 2.3. Typically, both γ rays and neutrons will be detected in the liquid scintillator neutron detectors, however pulse-shape-discrimination (PSD) can be used to distinguish the two types of radiation. More information on this procedure can be found in Chapter 4, Section 2.1.

Chapter 3

Experimental Campaign

The 2020 campaign at ANL aimed to perform a sequence of experiments exploiting high-resolution in-beam proton-γ spectroscopy near the proton drip line [2]. The campaign was divided into three main experiments: the first dealt with particle- and γ ray coincidence spectroscopy of ^{57}Cu [2], the second experiment was aimed at studying isospin symmetry and proton decay in the upper *fp*-shell by looking at $A = 61, 62$ nuclides [15], and the third experiment was aimed at proton- and γ-ray spectroscopy of ^{65}As [16]. This thesis deals exclusively with the second experiment. The aim of this chapter is to provide an overview of the experiment and illustrate the experimental setup, as well as describe its components.

1 Fusion-Evaporation Reactions

There are many ways accelerated nuclei can interact with stationary nuclei in the target. They can scatter, undergo Coulomb excitation reactions, deep inelastic collisions, fragmentation, and fusion. Fusion evaporation is the most probable reaction type for low-energy, central interactions between nuclei. Typically, the beam-ion energies range between 3 and 5 MeV per nucleon. During a fusion-evaporation reaction, the nucleus from an incident beam hits a stationary target nucleus and forms a compound nucleus. This compound nucleus is highly unstable because it is in a highly excited state and has a very high angular momentum. It has a very short lifetime, on the order of 10^{-19} seconds. To descend to a lower-energy state, it decays by emitting various particles such as α particles, protons, or neutrons, which are said to be "evaporated". After a certain point, it is no longer energetically favourable to decay by means of evaporating particles, passing the particle evaporation threshold. The remaining system will emit statistical γ rays, until the yrast line is reached. This is visualised in Figure 3.1. The yrast line denotes the highest angular momentum per excitation energy of a nucleus, which then de-excites by emission of discrete γ rays. These discrete γ rays are of great interest when studying nuclear structure, because they correspond to the differences in energy levels within the nucleus, allowing us to to map out level schemes. According to Bohr's independence hypothesis, the products from the compound nucleus are distributed isotropically in all angles, and the probability of a specific decay mode is unaffected by the formation mode of the nucleus.

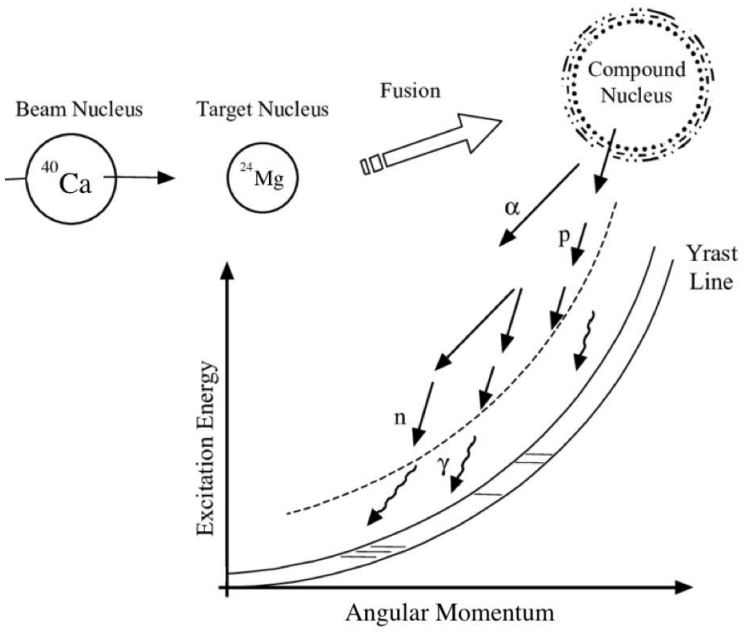

Figure 3.1: Diagram illustrating the decay of a compound nucleus. It de-excites through the emission of particles such as protons, α particles, and neutrons. The dotted line marks the particle evaporation threshold, and when crossed the nucleus will begin to de-excite by statistical γ rays, until the yrast line is reached. The yrast line indicates the highest angular momentum for a given excitation energy of a nucleus. After this point the remaining nucleus will reach the ground state by emitting γ rays with discrete energies [17].

In this experiment, a ^{40}Ca beam at an energy of 106MeV was used to bombard a ^{24}Mg target, leading to a heavy-ion fusion-evaporation reaction ^{40}Ca + ^{24}Mg $\rightarrow$ ^{64}Ge*. The target was made of 0.4 mg/cm^2 thick, self supporting target foil of highly enriched ^{24}Mg. The Argonne Tandem Linac Accelerator System (ATLAS) was used to provide the ^{40}Ca ion beam. One of the aims is to study excited states of ^{62}Ge, which is produced in one of the five reaction channels illustrated in Figure 3.2. The cross-sections of the channels depend on the statistical probabilities of which particles are evaporated, which depends on how much energy the initial system contains.

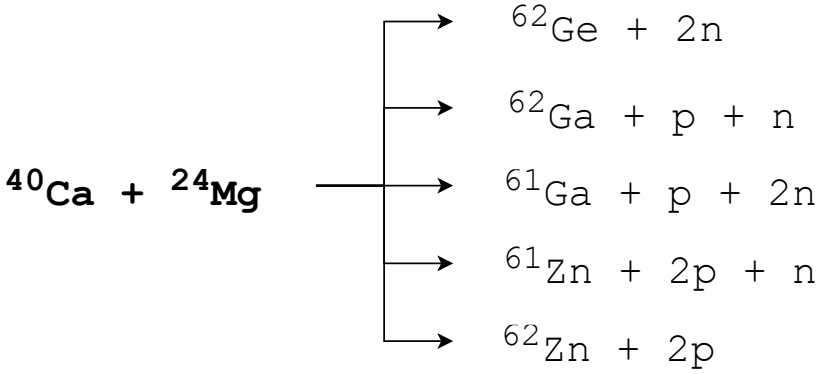

Figure 3.2: The five reaction channels of interest in this experiment, out of ≈20 different residual nuclei produced in total.

2 Experimental Setup

Performing studies near the proton drip line can be challenging because the cross-sections for producing such nuclei are very low. This means that the rare γ rays emitted from these nuclei can be obscured by γ rays from isotopes with much higher production cross-sections. As a result, one must use a combination of different detectors along with the Fragment Mass Analyser (FMA) to perform coincidence measurements. Some modifications were implemented in the MICROBALL and GAMMASPHERE detectors. Two CD-type DSSDs were installed into MICROBALL and the 30 foremost HPGe detectors of GAMMASPHERE were replaced by the Neutron Shell. Finally, the FMA was set to analyse nuclei with mass numbers $A = 60, 61, 62$. Their mass-to-charge ratio, A/Q was determined with the a Parallel Plate Avalanche Counter (PPAC) [6], and information on their proton number, Z, was gathered via an Ionisation Chamber (IC). Furthermore, with the present setup, one can measure coincidences between γ rays and recoils, as well as coincidence between γ rays and evaporated particles. The former allows A and Z identification, and the latter allows for reaction-channel selection.

The full experimental setup contains multiple detectors; some of these include GAMMASPHERE, MICROBALL, Neutron Shell, PPAC, and the Ionisation Chamber (IC). The configuration of the detectors is shown in Figure 3.3. Each of the major hardware components is described in more detail in the following sections of this chapter.

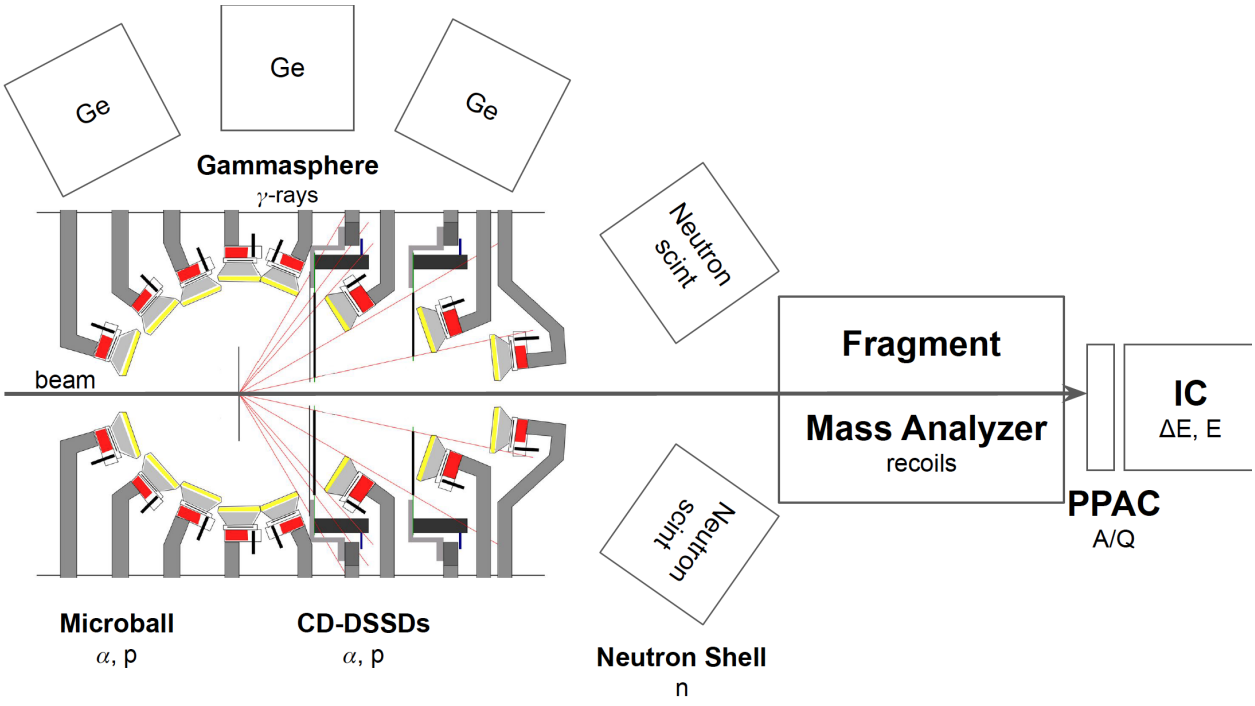

Figure 3.3: Schematic diagram of the complete experimental setup showing the arrangement of all detectors (not to scale) [18].

2.1 GAMMASPHERE

GAMMAPHERE is a γ-ray spectrometer composed of up to 110 High-Purity Germanium (HPGe) n-type coaxial detectors arranged in a 4π configuration [4]. It is currently situated at ANL, Chicago, where it is used for collecting data from mostly fusion-evaporation reactions, aiding nuclear structure research on nuclei far from the line of stability. It was designed with a purpose of achieving higher efficiency, energy resolution, and higher peak-to-total ratio than its predecessors. The Compton suppression shield for each crystal is made out of seven BGO scintillator detectors, where six form a hexagonal shield array around the HPGe crystal, and one is placed directly behind it as seen in Figure 3.4. The Hevimet absorbers were removed in the 2020 campaign to allow for γ-ray multiplicity and sum energy measurements [2]. Liquid nitrogen dewars are used to cool the GAMMASPHERE detector modules. 69 out of 110 detectors were in use during this experiment, where 30 out of the 110 positions were occupied with neutron detectors instead. More details about the neutron detectors can be found in Section 2.3.

Figure 3.4: A schematic drawing showing the side-view design of GAMMASPHERE [19].

2.2 MICROBALL + Si Detectors

MICROBALL is an ancillary detector used in combination with GAMMASPHERE, developed by Washington University, St. Louis. It is a nearly 4π detector made up of 95 closely packed Caesium-Iodide Thallium activated CsI(Tl) scintillator detectors. It is used to detect light charged particles such as α particles and protons. MICROBALL allows for the charge specific selection of reaction channels, to determine the recoil direction of the product nuclei using their measured momenta. This allows for more precise Doppler corrections to be made which can improve the energy resolution of GAMMASPHERE by up to a factor of three [19].

In the present experiment, a single ring (ring 4 with 12 CsI elements) is removed and replaced by two CD-type DSSDs, as seen in Figure 3.3. This was done to make significant improvements to the granularity of the charged-particle detector system, for charged particle spectroscopy and to add tracking capabilities to distinguish the interaction points. Each CD-DSSD contains 32 rings and 64 sectors, providing a granularity of 2×2048 pixels, requiring 192 readout channels (2×96) [2]. The way MICROBALL was situated inside GAMMASPHERE is photographed below in Figure 3.5, with the beam entering from the right hand side.

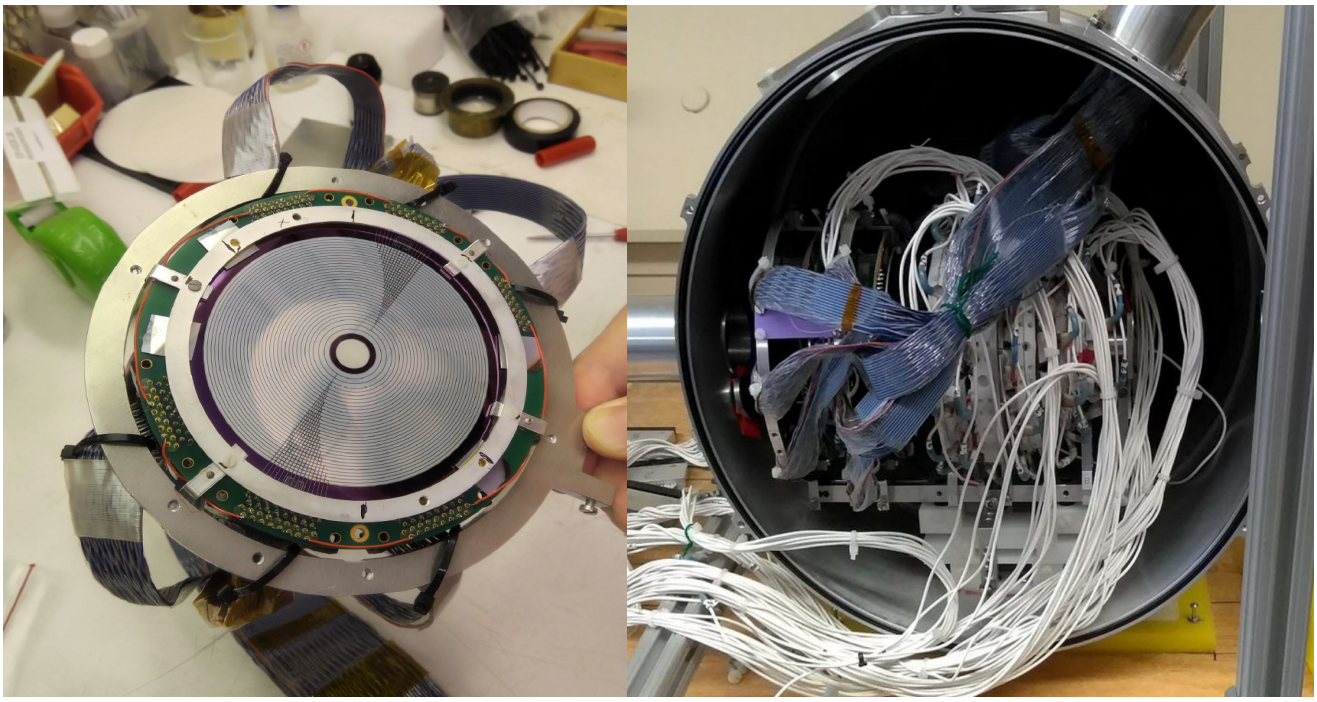

Figure 3.5: (Left) Photograph of a single CD-type DSSD. (Right) Photograph of the complete assembled MICROBALL detector ready to be placed inside GAMMAPHERE [20].

2.3 Neutron Shell

The Neutron Shell was developed specifically for use in conjunction with GAMMASPHERE with a purpose for selecting one- and two- neutron evaporation channels. Since it is of interest to study weak $2n$-evaporation channels, it is necessary for a neutron detector to be part of the setup. It comprises 30 tapered hexagonal liquid scintillator detectors which replace 30 GAMMASPHERE modules at forward angles with respect to the beam direction. BC501A, an organic scintillator liquid was used to fill the modules [21].

2.4 Fragment Mass Analyser

Identification of the nuclear reaction products, referred to as "recoils" in this section, is an imperative part of the process when trying to investigate coincidences between γ rays and a given isotope. This section aims to describe the Fragment Mass Analyser (FMA) and Parallel Plate Avalanche Counter (PPAC) used for mass discrimination of recoils.

The FMA is an eight meter long recoil mass spectrometer located at the ATLAS accelerator in ANL. Its primary function is to separate nuclear reaction products from the heavy-ion beam and disperse them according to their mass-to-charge ratios (A/Q). This is done with the help of magnetic and electric fields. The FMA consists of four magnetic quadrupoles (Q1, Q2, Q3, and Q4), two electric dipoles (ED1 and ED2) and one magnetic dipole (MD) as seen in the schematic in Figure 3.6 [6]. When used in combination with GAMMASPHERE it is possible to correlate prompt γ rays with the recoils detected with an ancillary detector, in this case the PPAC and IC combination (described in more detail in section 2.5). These are placed at the final focal plane. When the recoils first enter the FMA, the nuclear reaction products are separated from the incident beam by their difference in momentum, P/Q. Next, the recoils are further separated according to their mass-over-charge ratio, A/Q, independent of energy. The focusing parameters of the magnets used can be adjusted to suit different kinds of experiments, for example to optimise A and Z number separations for various beam energies. The x- and y- positions of the recoil products in the focal plane is measured using the PPAC. The recoils then continue their trajectory until they are stopped in the IC.

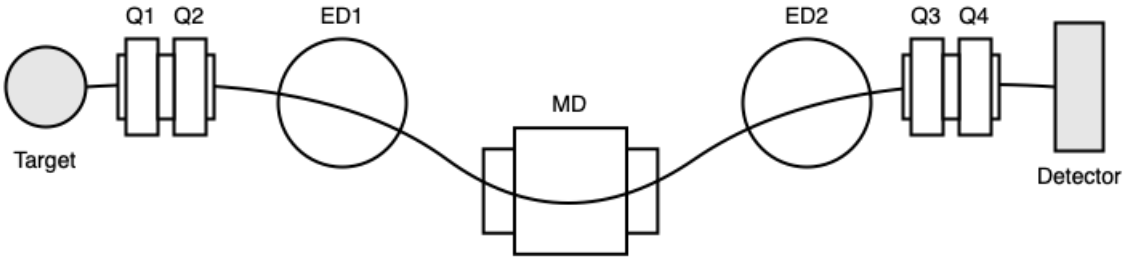

Figure 3.6: Schematic diagram of the FMA. Q1-Q4 are quadrupole magnets, ED denotes an electric dipole, and MD is a magnetic dipole. The detector in this case consists of the PPAC and IC. Adapted from [6].

2.5 Ionisation Chamber

Using the FMA alone, one is only able to deduce the recoil's mass number, A. An Ionisation Chamber was used to further separate the recoils during the experimental campaign by Z number based on energy losses. The aim of this part of the setup is to completely stop the incoming recoils from the FMA in order to deduce their energy and energy loss.

The working principle of an IC relies on ionisation in the gas medium caused by incoming radiation. There is a potential difference applied across the detector such that charges (i.e. ion - electron pairs) can travel towards the cathode or anode. This makes it possible to detect an electric current, and hence detect incoming particles. The volume of the gas within the IC stays constant, and so for a constant rate of radiation, the rate of ionisation is also constant. This means that the produced current will be proportional to the ionisation rate of the gas, allowing us to determine the energy of the incoming particles [22].

The IC used in this experiment is segmented into three main parts, and each part can detect the energy loss independently. The amount of energy deposited in each part of the IC depends on the Z number of the recoil. The total energy loss of an ion can be deduced from adding all the energy losses in each part. This is because a heavier nucleus will lose more energy in the first part of the IC and a lighter nucleus will lose most of its energy in the third part. This can be motivated by the Bethe-Bloch formula shown in equation 2.4. Hence, energy-loss functions can be constructed by using different combinations of the energy losses in each part of the IC. More details about energy-loss functions can be found in Chapter 2.5, Section 5.2. Based on such measurements, one can add the energy loss in each section and gain information on the recoil's Z number.

Chapter 4

Data Handling

During the experiment, data was collected in chunks referred to as runs, spanning over roughly one hour each. This was done as a safety measure to prevent larger amounts of data from becoming corrupted in case of something going wrong. It is also helpful to have compartmentalized data to allow for easier processing and eventually comparing different settings during the experiment. 161 runs were collected for this experiment, amounting to roughly seven Terabytes of raw data in total. The runs were grouped into "subsets" based on similar experimental conditions. Before a scientific analysis can take place, the raw data must be processed. This chapter aims to describe the steps taken to prepare the data for further analysis. Three separate DAQs were used in this experiment: Digital GAMMASPHERE (DGS), Digital Fragment Mass Analyser (DFMA), and the Washington University DAQ (WUDAQ). All data handling was performed on Aurora [23], a cluster resource on LUNARC [24], the centre for scientific and technical computing at Lund University.

Data Merging and Sorting

Data merging and sorting was done using `GEBMerge` [25] and `GEBSort` [25], analysis codes developed at ANL. The codes are written in ROOT [26], a data-analysis framework developed by CERN [27], as well as C and C++. Since several DAQ systems were used to acquire data, the first step in the data processing stage was to merge all raw data belonging to a single run from all three DAQs. This was done with the help of `GEBMerge`, which combines all hexadecimal data files and orders the events according to timestamps. After the merged file is obtained, it is sorted using the `GEBSort` code, which produces a `.root` file. `GEBSort` constructs the events in a way where all the timestamps within a 8 μs window are selected. Each of the events are decomposed into subevents according to their data type. `GEBSort` is made up of several main parts, each of which correspond to a detector system or analysis stage. Each subevent is processed by the relevant part of the code, and "hits" are created. Each hit has parameters such as energy, time stamp, and detector identification associated with it. The analysis can then be programmed by sorting the hits from events into histograms which are saved into `.root` file format. These histograms are used to help process data and also perform final analysis. It is worth noting that GAMMASPHERE data is of significant importance, because a lot of time correlations are performed.

1 Analysis Methods

The complex experimental setup allows for different methods of selecting reaction channels. In the case of ^{62}Ge nuclei, there are two main methods available for finding relevant γ coincidences. These methods are illustrated in Figure 4.1. Since ^{62}Ge is created through a $2n$ reaction channel, it is expected that no charge particles are detected. Both approaches involve using the MICROBALL and Si detectors as veto detectors for charged particles (α-particles and protons) and the FMA to select $A = 62$. In order to discriminate γ rays from the reaction channel of interest in this thesis, ^{64}Ge* $\rightarrow$ ^{62}Ge + $2n$, it is a requirement that at least one neutron, but no charged particles and mass $A = 62$ are detected. In Method 1, the Neutron Shell is used to select the $2n$ channel as previously mentioned. In Method 2, the IC is used to select the nucleus with the desired Z number. The rest of this chapter aims to discuss the two different approaches in greater detail as well as how they were used in this thesis.

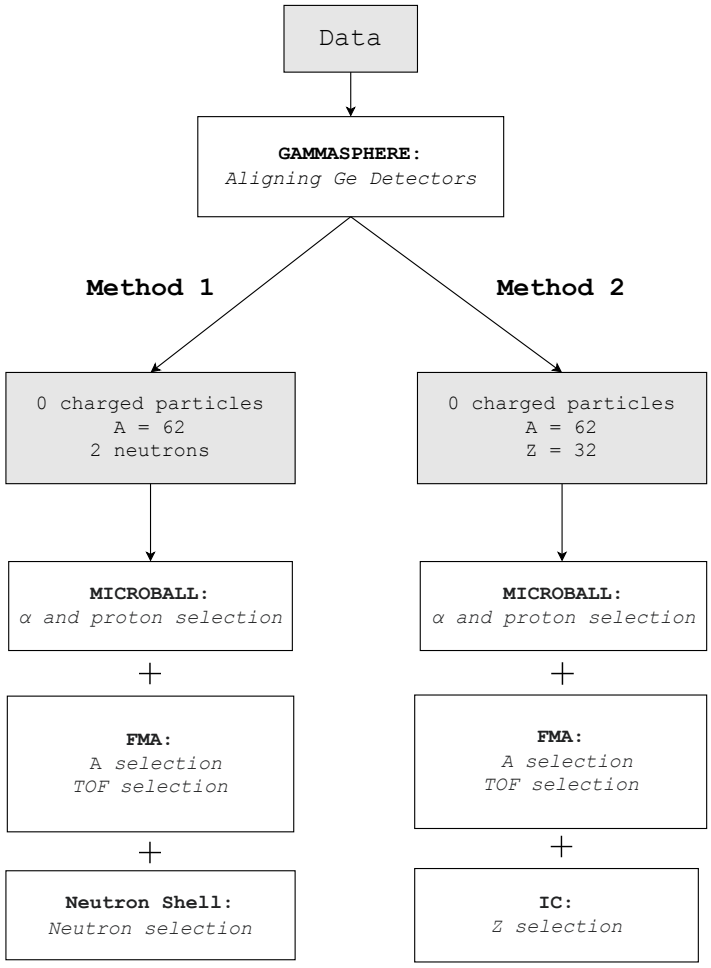

Figure 4.1: Flow chart illustrating the possible methods of selecting the ^{62}Ge production channel with the current experimental setup.

2 GAMMASPHERE: Data Preparation

2.1 Doppler Correction

When the incident nuclei hit the target and undergo fusion, they recoil, inducing a Doppler shift in the emitted γ rays. In case their velocity, v, is much smaller than the speed of light, c, the Doppler shift can be calculated according to equation (3.1). Here E_γ is the γ ray's measured energy, $E_{\gamma 0}$ is its true energy. The latter is the case for practically all recoils reaching the focal plane of the FMA.

$$E_\gamma = E_{\gamma 0}(1 + \frac{v}{c}\cos\theta) \tag{4.1}$$

2.2 Energy Calibration

HPGe detectors can have varying responses to the same γ-ray energies. Therefore, they must be calibrated in energy. A preliminary calibration was done during the experiment which was used during beam time. However, this needs to be further improved upon. In total, three rounds of calibrations were done for all 69 detectors: the preliminary online base calibration, a calibration with a source, and in-beam data calibrations for subsets of experimental data.

For the first round of calibrations carried out in this thesis, a ^{152}Eu calibration source was used since it contained peaks with well known and defined energies, which span over the relevant energy range. Data from other calibration sources, ^{207}Bi and ^{182}Ta, was also collected but was not used in the energy calibration. This is because the ^{182}Ta source contained insufficient statistics, and due to the opening and closing of GAMMASPHERE while replacing the sources, a number of detectors showed a significant difference in response. The peaks chosen from the ^{152}Eu spectrum were: 121.8 keV, 244.7 keV, 344.3 keV, 511.0 keV, 778.9 keV, 964.1 keV, 1112.1 keV and 1408.0 keV. A Gaussian curve was fitted to the selected energy peaks with a program called `HDTV` [28], a nuclear spectroscopy tool developed by the University of Cologne. The peak positions were extracted from the fit into an `ASCII` file. A linear calibration was used and considered sufficient, as the majority of detectors were within 1 keV of a given energy. This was verified with a `python` script. The calibration file containing calibration coefficients k and m was produced with a script written in `python`, using the `pandas` package. As a test for the next round of calibration, a following calibration file was produced for ^{207}Bi and applied on top of the ^{152}Eu calibration. This was tested with the ^{207}Bi data in order to verify that such a calibration procedure works properly before moving on to the in-beam data.

The next step is to calibrate the detectors with the in-beam data. Three peaks were selected, 136.6 keV, which arises from a Coulomb excitation from the ^{181}Ta absorbers placed in front of the DSSDs, 511.0 keV coming from positron-electron annihilation, and the Doppler shifted 1732.3 keV transition from the de-excitation of ^{61}Cu. Two linear calibrations were done for every subset, one for the part of the energy spectrum below 511 keV, and one for the higher energy part, above 511 keV. Two calibration files were produced for each subset, with the help of a modified `python` script to appropriately account for Doppler corrections. During this

stage, detectors 85, and 89 were switched off due to bad energy resolution. The mapping of all detectors was also cross-checked and corrected if necessary. In some cases, the subsets were also modified and split up further, in order to match more similar experimental conditions and variations in detector response. Once all the calibration files were implemented into the `GEBSort` code, histograms were used to visualise detector alignment for each subset, as seen in Figure 4.2. Misaligned detectors were investigated further and corrected if necessary.

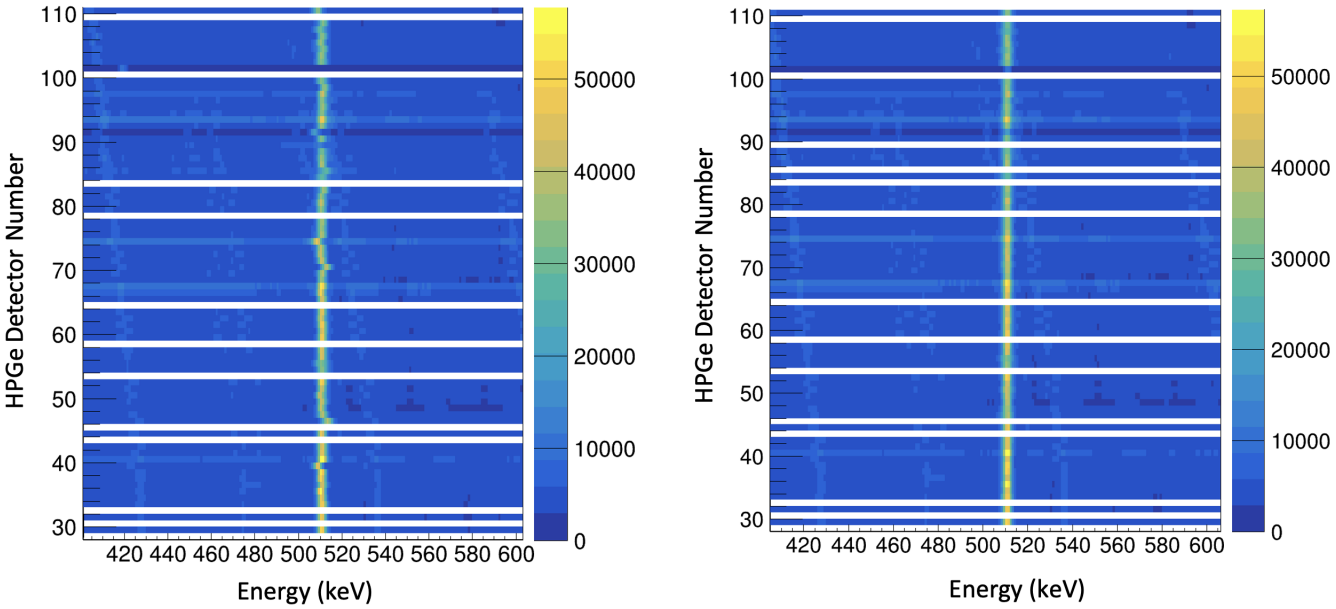

Figure 4.2: The 511 keV peak for all GAMMASPHERE detectors for the sample subset. The HPGe module number is on the y-axis with channel number on the x-axis. The figure to the left shows the alignment of the 511 keV peak with only the online base calibration and source calibration, whereas the figure on the right shows the alignment after a third round of in-beam data calibration was applied.

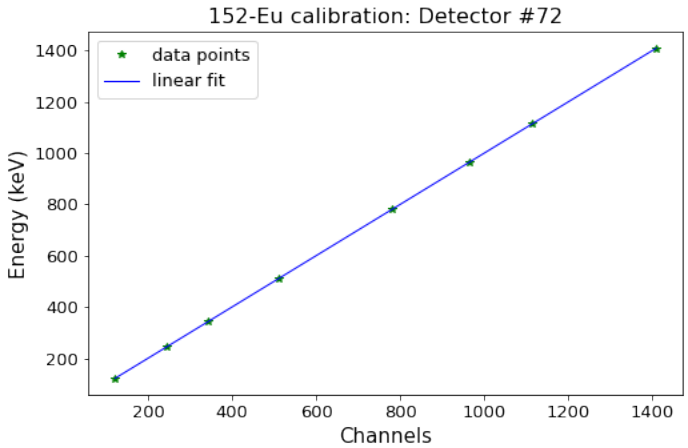

Figure 4.3: Energy calibration line produced with a ^{152}Eu source for a typical GAMMASPHERE detector.

2.3 Efficiency Calibration

The detected γ rays have varying efficiency depending on their energies, therefore an efficiency calibration of the HPGe detectors must be carried out. ^{152}Eu, ^{207}Bi, and ^{182}Ta were the sources were used, as they provide well defined peaks with energies spawning over a relevant region.

A program called `effit` [29] was used to perform the efficiency calibration. It reads the relevant peak intensities of selected peaks and compares them to tabulated values. The curve is then fitted with Equation 4.2. The parameters for all rings can be found in Table 6.1 in the Appendix.

$$\epsilon = \exp\left[(A + Bx + Cx^2)^{-G} + (D + Ey + Fy^2)^{-G}\right]^{\frac{1}{-G}} \tag{4.2}$$

Where $x = \log(E/E1)$ and $y = \log(E/E2)$ with E being the γ ray energy and $E1$ and $E2$ being constants having values of 100 keV and 1 MeV respectively. G is the interaction parameter; the sharper the turn at the top of the efficiency curve, the larger G will be [29].

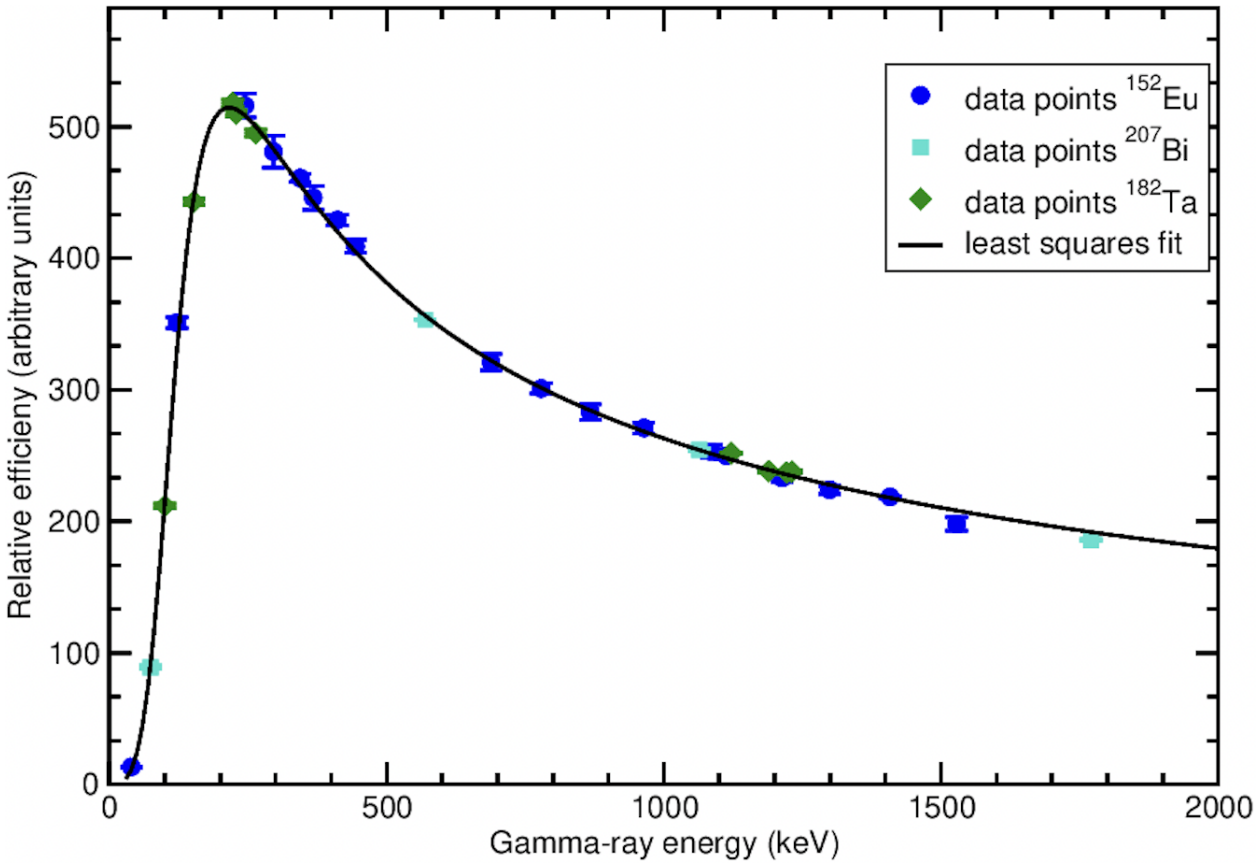

Figure 4.4: Efficiency curve for all the rings fitted to the data points of ^{152}Eu, ^{207}Bi and ^{182}Ta.

3 Reaction Channel Selection

The general approach when dealing with large amounts of data is to optimise all calibration and particle discrimination procedures on a given subset of runs, before proceeding to move on to following subsets. This section aims to describe the procedure of neutron and charged-particle discrimination.

3.1 Charged Particle Discrimination

Microball

Proton and α-particle discrimination in this experiment is done with the use of MICROBALL and DSSDs. For the purposes of this thesis, it is necessary to filter out the reaction channels which contain charged particles. Therefore, proton and α-particle discrimination is performed for anti-coincidence. Since the protons are lighter than the α particles, it is possible to create histograms where one can visually distinguish the two. This energy dependence of particles can be seen in Figure 4.5. It is then possible to draw a two dimensional region to select the particles of interest. These regions are referred to as "gates" in the rest of the text.

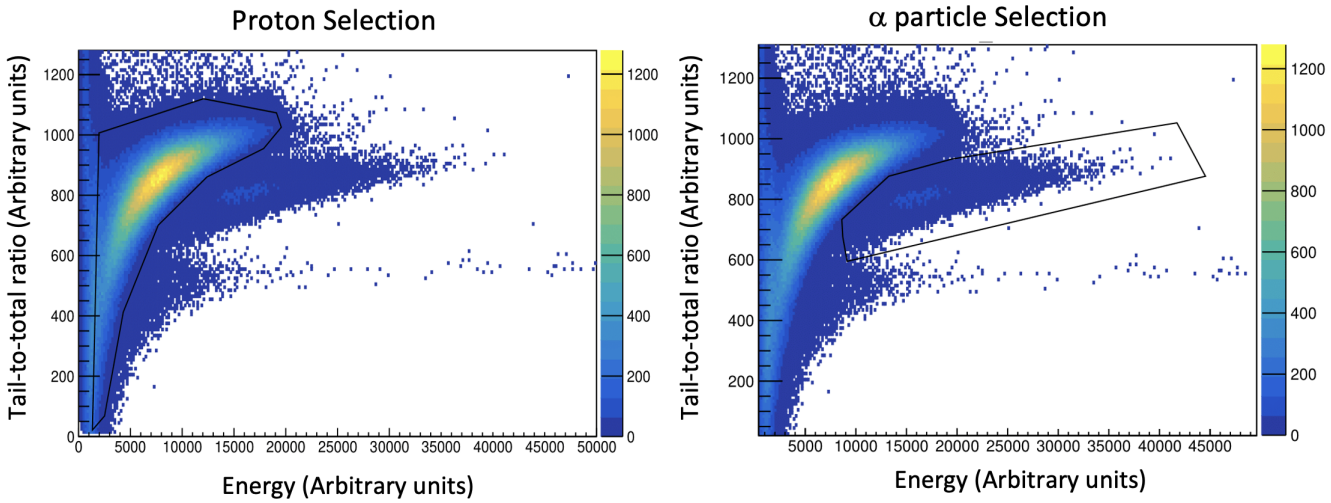

Figure 4.5: Both histograms have the total energy on the x-axis and the ratio of the tail-to-total energy on the y-axis for a typical MICROBALL Detector CsI detector, in this case detector number 1. The α particles and protons are enclosed in two-dimensional regions in the left and right panels, respectively.

Once the gates selecting α particles and protons are implemented for all MICROBALL detectors for the sample subset, it must be verified that the histograms did not move considerably for the following subsets. This can be due to changes in experimental conditions or fine tuning settings during the experiment. A check was done by visualising the two dimensional gates on top of the histograms for each subset. In this case, the aim is to select a reaction channel with zero charged particles, meaning the distinction of which particles are α particles and

which are protons is not of too much importance. The proton vs. α-particle separation for MICROBALL's CsI elements is currently being optimised. More details on this can be found in [30].

Silicon Detectors

Silicon detectors are an important part of the experimental setup used for tracking charged particles and proton spectroscopy. In the case of ^{62}Ge, they are simply used for vetoeing events similarly to MICROBALL. Preliminary proton and α-particle separation was done during beam time, and is considered sufficient for the purpose of this thesis.

3.2 Neutron Discrimination

Since both low-energy γ rays and neutrons are detected in liquid scintillator type neutron detectors, it is important to be able to distinguish them. There are four relevant parameters in this selection process: time, total energy, tail energy, and the ratio of the tail-to-total energy. Combinations of these four parameters can be plotted against each other to produce different histograms, for example the one in Figure 4.6. This shows the tail-to-total ratio vs. time. Similarly to the charged-particle discrimination process described in the previous section, it is possible to visually distinguish γ rays from neutrons. This is because γ rays travel at the speed of light such that they all reach the detectors at practically the same time relative to the time of the reaction, unlike neutrons which are slower and show a larger spread in energy and time. Three gates were implemented in total: neutron time vs. total energy, total energy vs. tail energy, neutron time vs. tail-to-total energy ratio (see Figure 4.6). If a subevent passes through all three gates, the detector subevent is declared a neutron and the whole event is chosen for further data analysis. This procedure was repeated for all neutron detectors.

Once the gates to select the neutrons are drawn and implemented into the sorting code, certain checks are performed to decide if they are optimised for the sample subset of runs. An efficiency of around 30% for the neutron detectors is expected, as well as minimal leak through of γ-ray events belonging to reaction channels without neutron evaporation. The efficiency of a neutron detector can be calculated with:

$$\epsilon_n = R/(1+R) \tag{4.3}$$

where ϵ_n is the neutron detection efficiency and R is a ratio obtained by comparing counts in a given peak between a neutron-gated spectrum and a control spectrum of γ rays stemming from reaction channels without neutron evaporation. For the sample subset, an efficiency of 31% was obtained, and the leak through was minimal. This can be seen in Figure 4.7.

Next, it was necessary to investigate whether the histograms have shifted for the following subsets of runs. This was done similarly to the proton and α particle selection described in the previous section, by visualising the gates for each subset. In this way, it was also possible to observe by how much the histograms shifted for each subset of runs. This was then used to shift the displaced histograms back into all three neutron gates for the affected subsets.

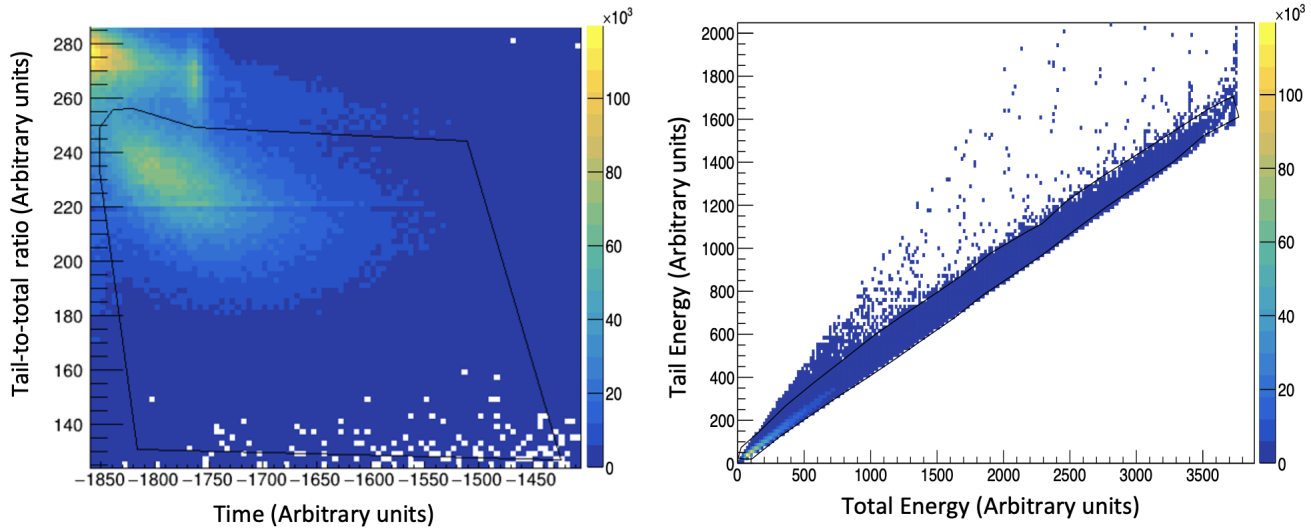

Figure 4.6: Examples of histograms used to distinguish γ rays and neutrons. The panel on the left shows the distribution of particles with respect to the tail-to-total ratio vs. neutron time, and the panel on the right shows total energy vs. tail energy. The outlines indicate two examples of gates drawn for a typical neutron detector (detector number 5) for the sample subset, in order to select events containing atleast one neutron. The right panel is already gated by the left panel.

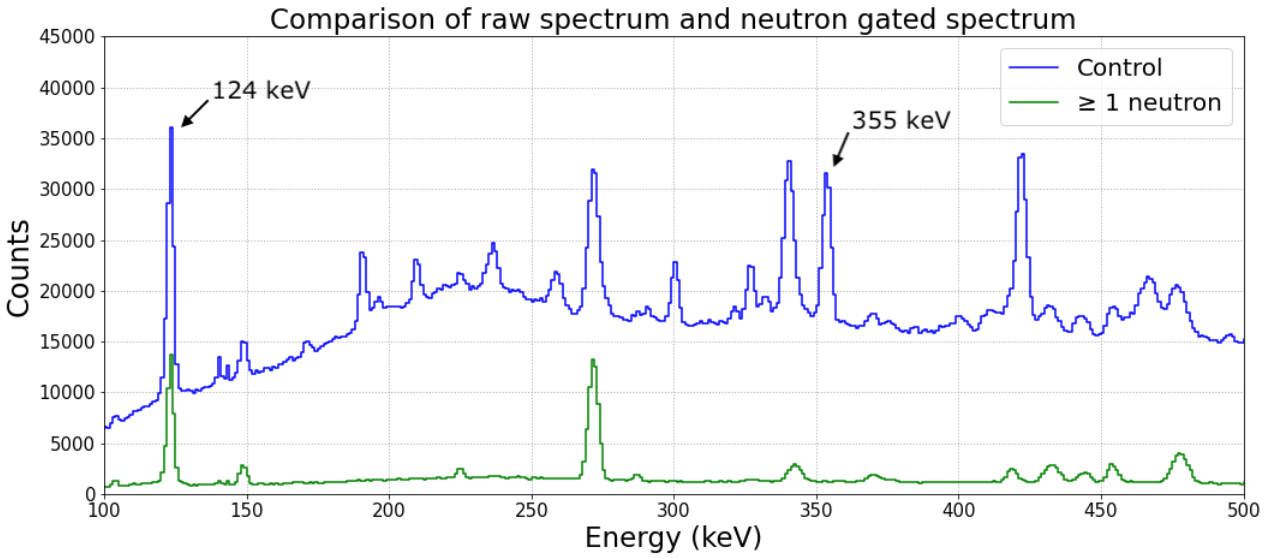

Figure 4.7: Histograms representing the number of γ ray counts with neutron gates (green) and without neutron gates (blue). The blue spectrum is the control spectrum, where one is able to see peaks around 124 keV (coming from ^{61}Zn, used for calculating efficiency of the neutron detectors) and 355 keV (arising from ^{61}Cu decay used to monitor charged particle leak through). In the green spectrum, it is clear that the 355 keV peak is sufficiently suppressed.

3.3 Missing Neutrons

During the process of performing the neutron discrimination as described above, overall low neutron statistics were discovered. It was observed that only 1/8 of the expected statistics were available in the neutron discriminated spectra. This issue was further investigated in detail, and it was discovered that only 1/4 of the anticipated neutron statistics were recorded during the experimental campaign. This was verified by cross checking the number of neutron events from the raw unmerged data (WUDAQ), as visualised in Figure 4.8. However, it was also discovered that half of the available neutrons were not correlated with any γ-ray events from DGS.

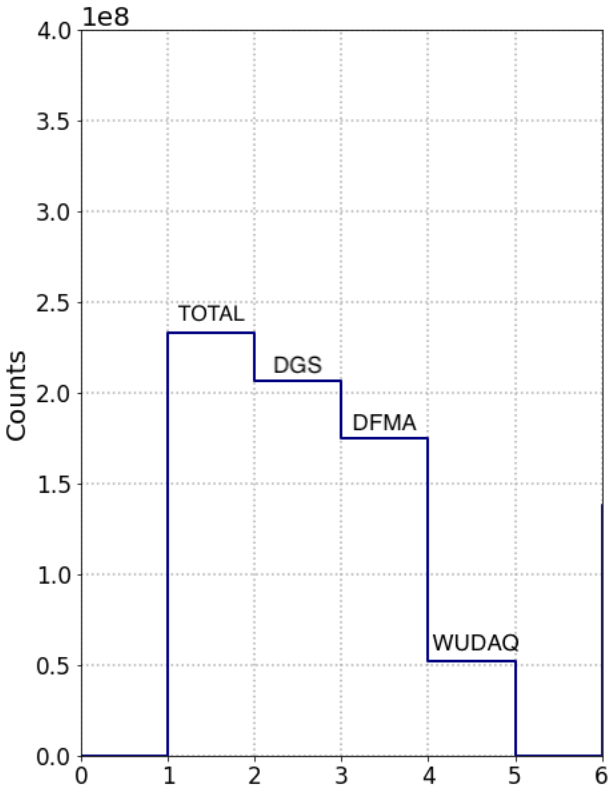

Figure 4.8: A comparison of WUDAQ and FMA event counts. The first bin contains the total number of events, the second bin contains the number of events with at least one DGS subevent, the third bin contains the number of events with at least one DFMA subevent and the fourth bin contains the number of events with at least one WUDAQ subevent. From this, it is possible to see that the number of WUDAQ events is much lower than the number of DFMA and DGS events.

These findings correlate with and explain why only 1/8 of the neutron data was observed and is available for further analysis at this stage. This issue is now being further investigated and attempts to recover some of these events will potentially be made by the co-supervisor of this project. Due to this unforeseen complication related to DAQ issues during the experiment, an attempt to select the ^{62}Ge nuclei was made with the second approach, Method 2, as illustrated in Figure 4.1.

4 Mass Selection

4.1 *A/Q*

For an experiment at a given beam energy, there is a certain probability that the recoils will be stripped of a certain number of electrons. The parameter Q denotes the charge state of a particle, which refers to the number of protons minus the number of electrons that are still bound to the nucleus [22]. Since this experiment was run at rather low beam energies, a value of $Q = 16$ was selected based on the probability of stripping the electrons off a $A = 62$ nucleus. The A/Q value can then be plotted against the atomic mass as shown in Figure 4.9. The FMA has an acceptance rate of $\pm 5\%$ in A/Q [6]. This is indicated by the dotted lines to the left and right of the centroid, representing the upper and lower level of acceptance. In this experiment the FMA was fine-tuned to accept recoils of $A = 62$ with $Q = 16$ and recoil energy, $E_{rec} = 54$ MeV [18].

4.2 Optimising Mass Selection

The PPAC provides us with a two dimensional position of the particle distributions. From Figure 4.9, it is possible to identify $A = 60$ and $A = 61$ from the plot. However, when selecting the masses of $A = 62$ and $A = 58$ one needs to be more careful as they are not so easily distinguishable. The aim is to get rid of as much of the ^{58}Ni contamination without reducing the number of ^{62}Ge counts significantly. As a start, the conditions for qualifying as $A = 58$ and $A = 62$ are set to be rather strict. Additional information can be deduced from plotting the total energy of the recoil against its time of flight (TOF). Due to the difference in mass, one can observe some separation and additional time-of-flight selection can be performed. With this, we require that for a recoil to be identified as $A = 58$ or $A = 62$ it must be gated by the both the mass gate as well as by the corresponding time-of-flight gate. A few iterations of the mass and time-of-flight gates were made to optimise them for the sample subset. The amount of ^{58}Ni leak through was monitored by observing the statistics of peaks at 1005 keV and 1454 keV, corresponding to the $4^+ \rightarrow 2^+ \rightarrow 0^+$ ground state cascade in ^{58}Ni.

4.3 Timing Coincidences

Certain one dimensional time gates are also implemented in order to select coincidences between detector systems. These coincidences include: DSSD and Gammasphere time gate, DSSD and Microball time gate, Microball and Gammasphere time gate, PPAC and Gammasphere time gate and Neutron Shell and Gammasphere time gate. These parameters are subset dependent due to variation in experimental conditions and settings. Therefore, these variables were reviewed for each subset and the coincidence selection was modified appropriately within `GEBSort`.

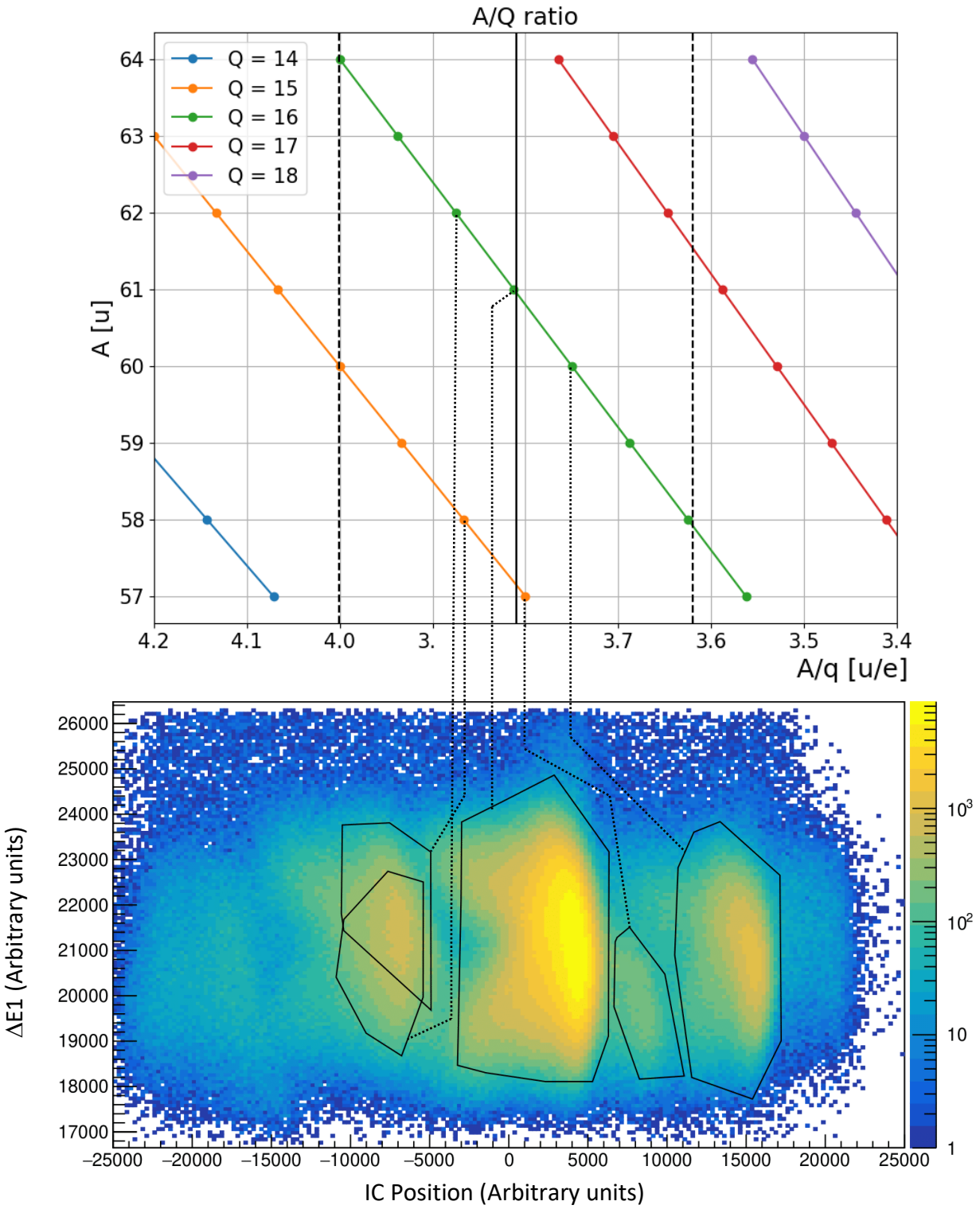

Figure 4.9: (Top) Plot displaying the masses of recoils vs. A/Q [18]. (Bottom) The dispersion of detected recoils in the A/Q focal plane in the first segment of the Ionisation Chamber. The dotted lines show the correspondence of the predicted positions of recoils in the IC according to their mass.

5 Ionisation Chamber: Data Preparation

5.1 Recoil Proton Number Selection

This is done with the help of the energy losses in the IC, section. The energy loss in each section of the IC can be plotted against the total energy of the ion. Since there are three sections in the IC, we have three energy losses, and hence we have three histograms of total energy vs. energy loss. These histograms are used to select the recoils using 2D gates. In order for a subevent to qualify as a recoil, it must be inside all three gates from the three different energy losses. These histograms also shifted during the experiment, and so new gates were drawn and implemented for the relevant subsets. Once only the recoils are selected, it is possible to select recoils of a certain mass. This is done by plotting the recoil masses against A/Q as seen in Figure 4.9 in Section 4.

5.2 Energy-Loss Functions

As mentioned in Chapter 3, Section 2.5, when an ion enters the IC, it deposits different amounts of energy in each part of the three segments of the chamber. The energy loss depends on the proton number, Z, of the ion. From this information, one can make various energy loss functions (ELFs), which are constructed by different combinations of the energies lost in each part of the chamber. By plotting the ELF against the recoil's total energy, it is possible to select the energy loss function which provides us with the best Z separation. In this thesis, several ELFs were considered, for instance:

$$ELF1 = \Delta E1 \quad ; \quad ELF2 = \Delta E1 + \Delta E2 \quad ; \quad ELF3 = \Delta E3 - \Delta E1 \tag{4.4}$$

By examining the ELF vs. total energy plots visually, it was deduced that $ELF3$ provided the most promising Z separation, and hence was selected for further optimisation. When an ion of a given charge state enters the IC, the energy loss in each part depends on its Z number. The amount of energy lost in the first segment increases with higher Z. Similarly, the energy loss of an ion in the second part of the chamber remains roughly constant with respect to Z number, and decreases in the third part. Due to this effect, it is reasonable to assume that the ELF which provides the best separation is one that combines information from both ΔE1 and ΔE3. According to Lise-Lotte Andersson's and Emma Johansson's Master theses, which dealt with a similar fusion-evaporation reaction [22] [8], this ELF was selected and gave the best Z resolution. More information about how this is further optimised can be found in Section 5.3.

The event-by-event total energy of the ion also affects the recoil's energy losses in the three sections, as can be seen in Figure 4.10. For this reason, it is important to normalise the ELF such that the the recoil's energy losses are independent of its total energy. This can be visualised by "straightening" the data as seen in Figure 4.11. This straightening procedure is done by selecting a few points on the slanted "banana", and fitting a parabolic curve to these points. Using the parameters from the fit, the distance of each data point on the graph to the parabolic function can be calculated. The distance of this can then be plotted against γ-ray energies to create a recoil-γ matrix, as seen in Section 5.

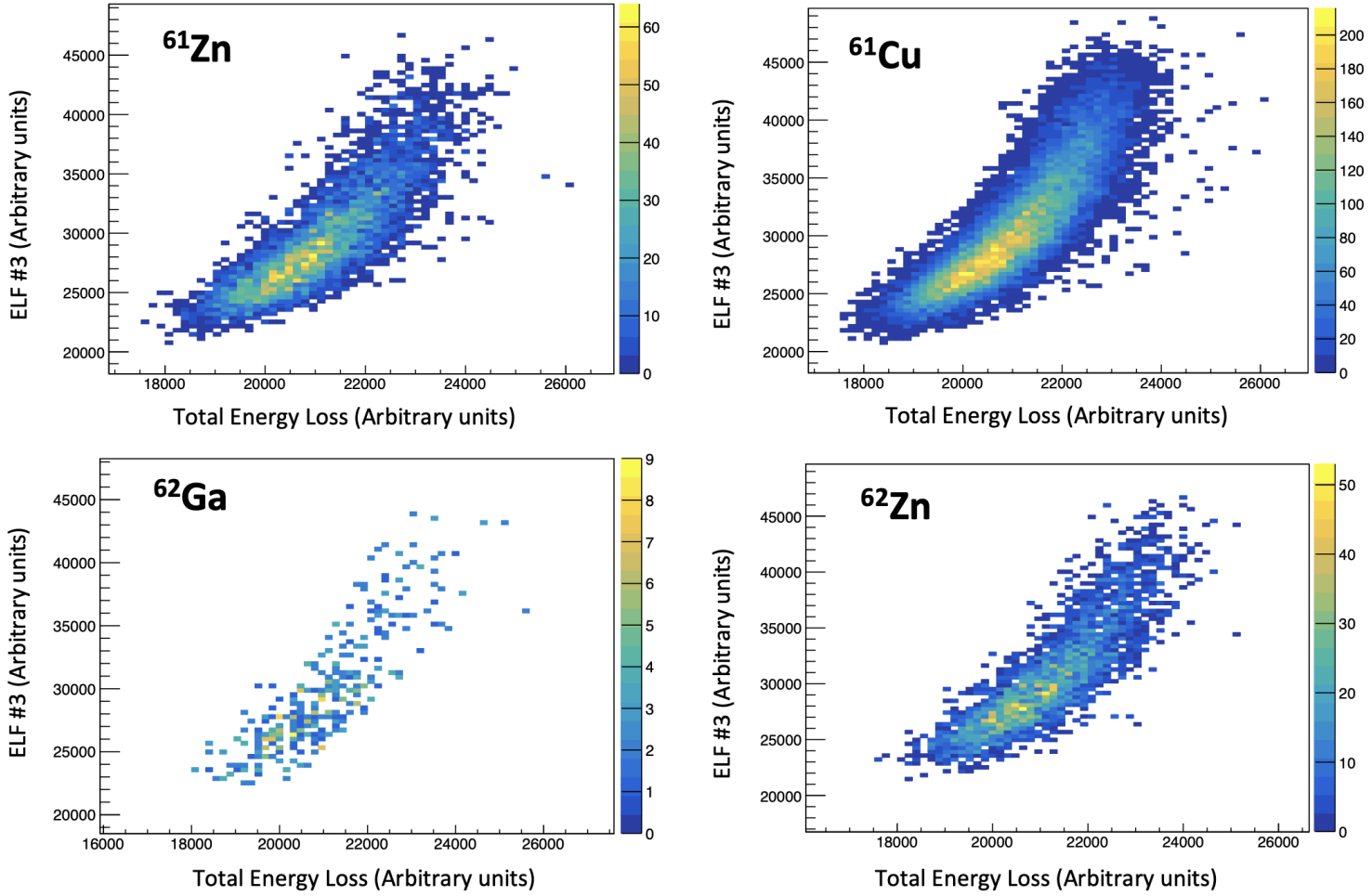

Figure 4.10: Uncorrected histograms showing total energy loss on the x-axis and ELF #3 on the y-axis, containing statistics from the first five subsets. Particle distributions for ^{61}Zn and ^{61}Cu shown in the top left and right figures respectively. Similarly, the particle distribution for ^{62}Ga is shown in the bottom left and ^{62}Zn in the bottom right corners. The ^{61}Cu plot was used when constructing the straightening function because it had the most statistics.

5.3 Optimising Z Separation

The general aim is to achieve the best possible Z resolution in the IC by optimising the energy loss function. Once this function has been selected, it can be further manipulated in order to attain an improved Z resolution. By looking at the Figures 4.10 the skew of the two "bananas" seems to be independent of mass. For this reason, the same straightening function is used for all different masses. The parabolic function was fitted to points selected from the ^{61}Cu plots because it contained the most statistics. However, after this was done, it was still possible to observe a further dependence between the total energy (x-axis) and $ELF3$ (y-axis) as seen on the left in Figure 4.11. Therefore, a trial was made to further straighten the banana by a creating a second parabola with points from ^{61}Cu in Figure 4.10 and obtaining new parameters. The effect of this second round of "straightening" can be seen on the right in Figure 4.11, where the data points appear to be in a fully horizontal position. It can also be noted that a similar dependence was observed in the ELF #3 time-of-flight vs. ΔE3 plot which was also corrected with this second iteration of straightening. This approach was assumed to generate the best level of Z separation in the recoil-γ matrix as of now, which is discussed further in Chapter 5, Section 1.

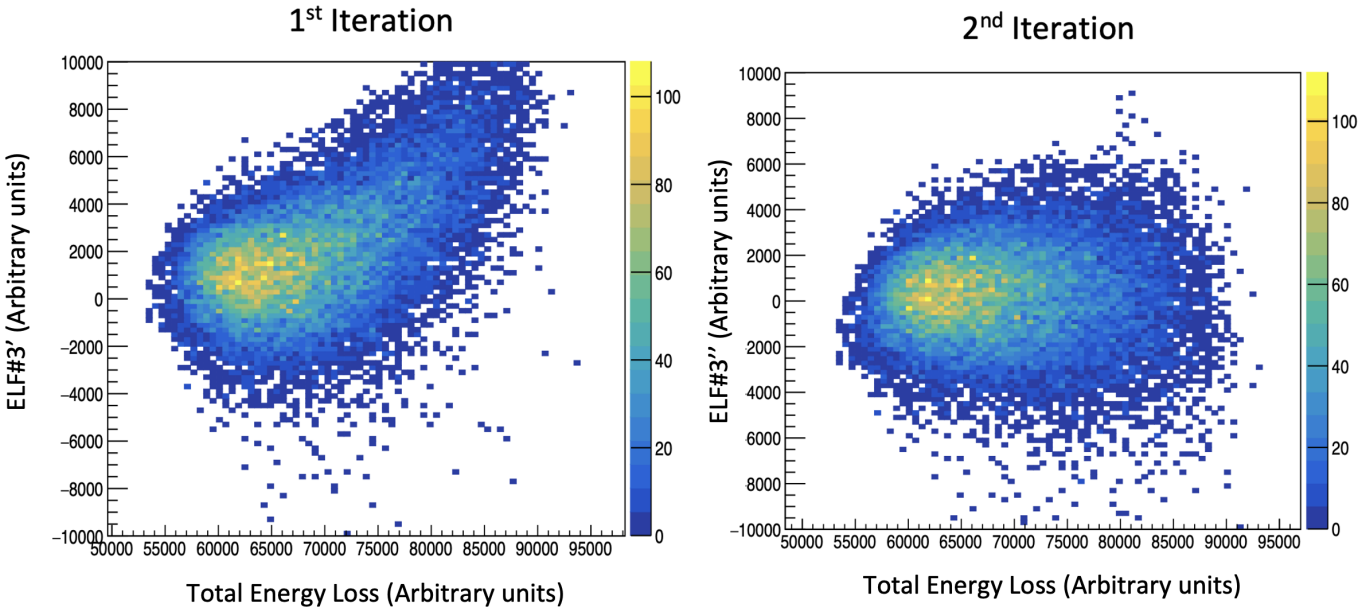

Figure 4.11: (Left) Figure showing the energy dependence of recoils on after the first round of straightening. As seen, there is still be some dependence between the quantities observed. (Right) Corrected histogram rotated into a horizontal position after the second iteration of straightening.

Chapter 5

Results and Discussion

1 The Recoil-γ Matrix

The recoil-γ matrix is constructed by plotting the selected ELF, in this case ELF #3" as a function of γ-ray energies. The recoil-γ matrix for $A = 62$ is shown in Figure 5.1, and the positions of peaks belonging to ^{58}Ni, ^{62}Zn and ^{62}Ga are indicated. It is possible to notice the separation between the $A = 62$ nuclei and the ^{58}Ni contamination, whose maximum peak positions sit significantly higher than that of $A = 62$ nuclei. The aim is to use the ELF which achieves the highest Z separation of the nuclei, which can be visualised by a displacement in positions of the peak maxima on the y-axis. In this way, one can separate ^{62}Zn and ^{62}Ga, from which it may be possible to distinguish the transitions belonging to ^{62}Ge with some additional analysis steps described in more detail in 3.1.

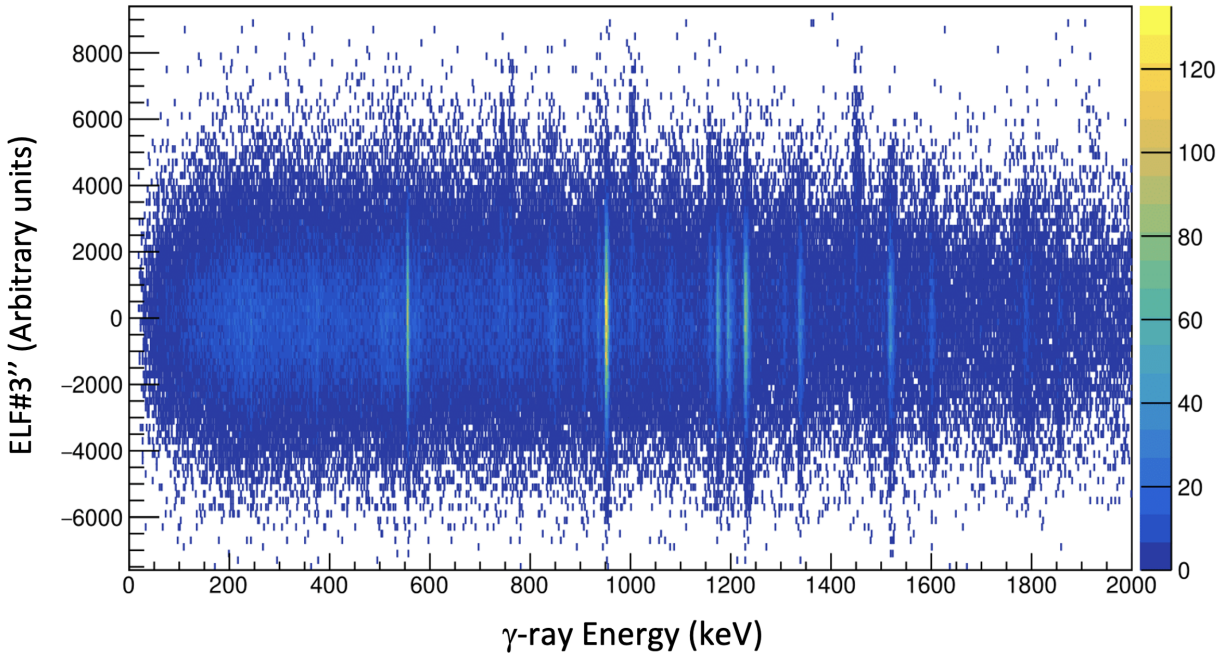

Figure 5.1: Recoil-γ matrix showing distribution of peaks in ^{62}Zn and ^{62}Ga nuclei.

2 Selecting the ELF

By plotting the ELF vs. γ-ray energies, it is possible to obtain the recoil-γ matrix as seen in the previous section. Two different recoil-γ matrices were produced to investigate the improvement of Z separation by using one or two iterations of the straightening procedure. The IC spectrum is produced by projecting the recoil-γ spectrum onto the y-axis. The IC spectrum in Figure 5.2 was created by selecting a region containing the main peak intensity of the $2^+ \rightarrow 0^+$ 954 keV ground state transition in ^{62}Zn. This peak was chosen because it was a intense γ-ray transition. It is possible to notice a slight tail on the right side of the green spectrum which is not so apparent in the red spectrum. The FWHM for each iteration was calculated. For the first iteration (green peak), the FWHM $\approx$ 4479. After the second iteration (red peak) the FWHM was calulated be be 4084. A smaller FWHM will allow for γ-ray spectra with a higher Z resolution, and so it can be argued that the second iteration is better.

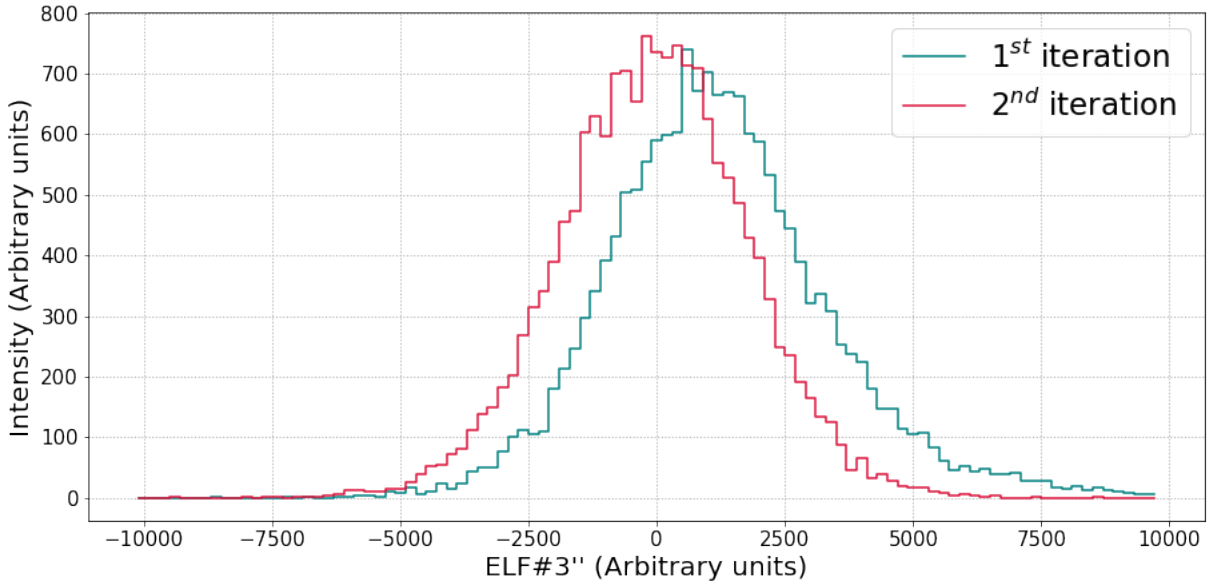

Figure 5.2: IC spectrum of for the γ rays belonging to the 954 keV transition in ^{62}Zn. The blue and green spectra show the IC spectrum after one and two iterations of straightening, respectively.

3 Gated Spectra

3.1 $A = 61$ Separation

Once an ELF function is selected, it is possible to generate IC spectra for each recoil, selected by processes described in Section 4. In this way, one can observe the Z separation of recoils. Since ^{62}Ga contains too few statistics (as seen in Figure 4.10), it is difficult to check if this discrimination works correctly. For this reason, nuclei of $A = 61$ were used to illustrate the Z separation for ELF #3", after the second iteration of straightening. This is done by projecting the 124 keV ^{61}Zn and 529 keV ^{61}Cu peaks, visible in the recoil-γ spectrum in Figure 5.1, onto the y-axis. Figure 5.3 demonstrates this comparison. It can be clearly seen that despite the observable separation, the ^{61}Zn spectrum will still contain peaks from ^{61}Cu and vice versa.

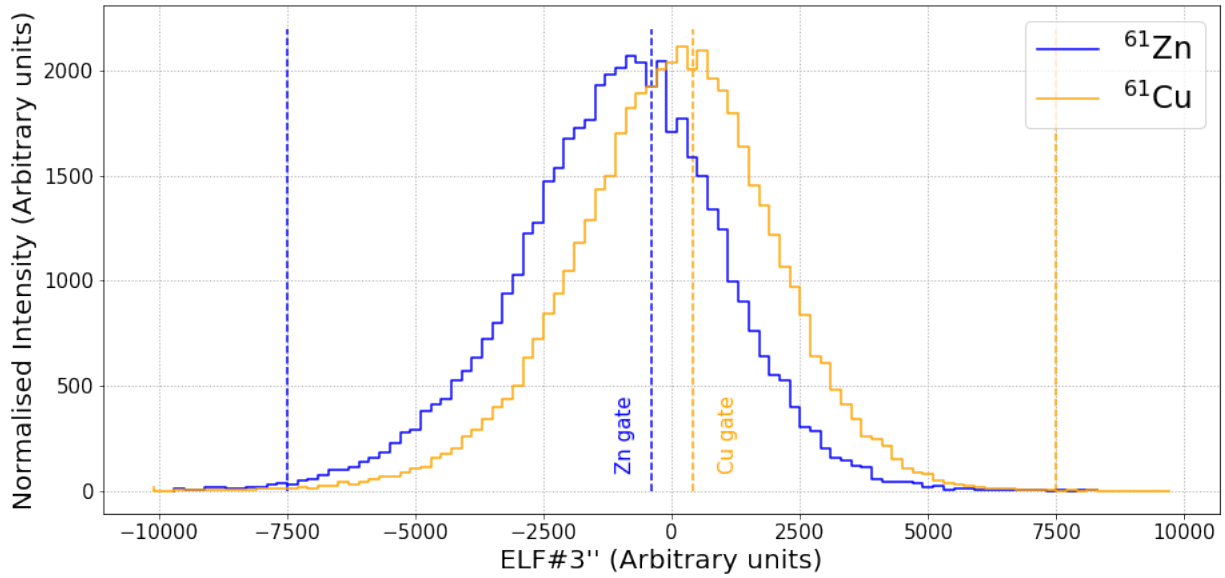

Figure 5.3: Figure showing the IC spectrum for ^{61}Zn (blue) and ^{61}Cu (orange) after the second iteration of straightening ELF #3. The dotted lines in their respective colours indicate where it is possible to gate on the spectra.

To test the Z separation further, one needs to look at the cleaned ^{61}Zn spectrum. By using the gates illustrated in Figure 5.3, It is possible to project the recoil-γ matrix onto the x-axis to obtain the ^{61}Zn spectrum, which will also contain peaks from other $A = 61$ nuclei, mainly ^{61}Cu. Both the ^{61}Zn and ^{61}Cu γ ray spectra can be seen in Figure 5.4. The procedure to obtain a clean ^{61}Zn contains two main steps: (1) the intensity if the peaks from the ^{61}Cu spectrum must be normalised to those in the ^{61}Zn spectrum, and (2) the normalised ^{61}Cu spectrum must be subtracted from the ^{61}Zn spectrum, leaving only the ^{61}Zn γ rays behind. The vice versa can be done to obtain a clean ^{61}Cu spectrum. The cleaned spectrum of ^{61}Zn can be seen in Figure 5.5. By examining the peaks, it is possible to confirm that they are in

fact known intense transitions belonging to ^{61}Zn.

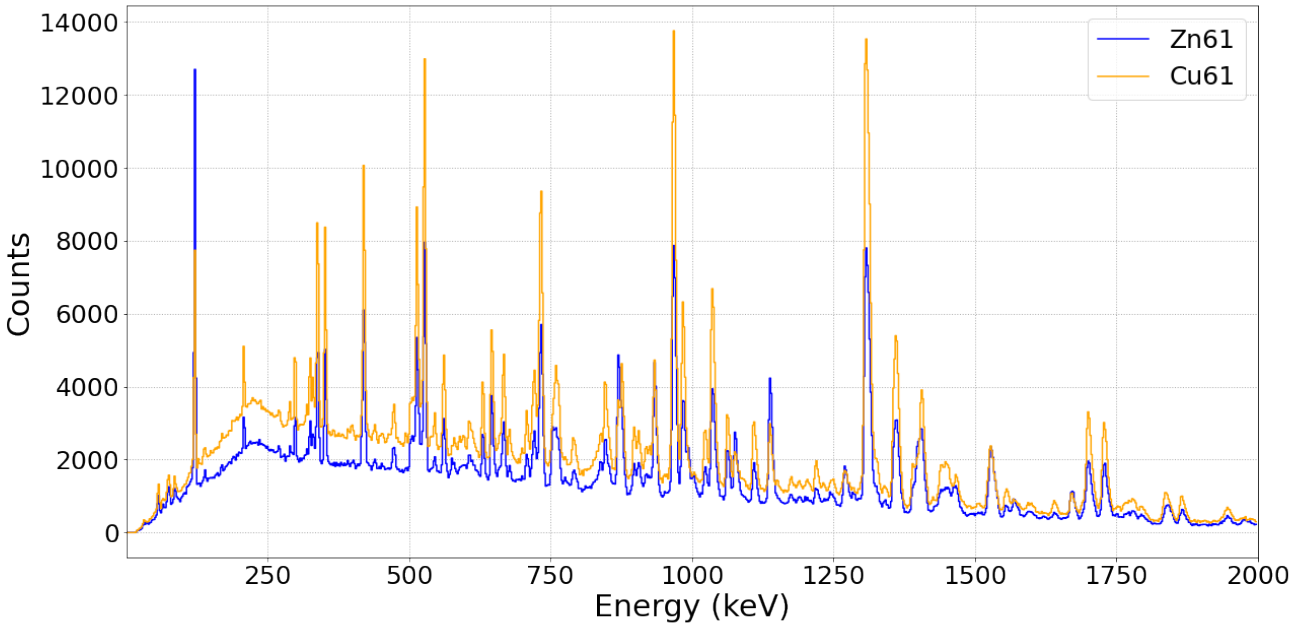

Figure 5.4: ^{61}Zn (blue) and ^{61}Cu (orange) γ ray spectra.

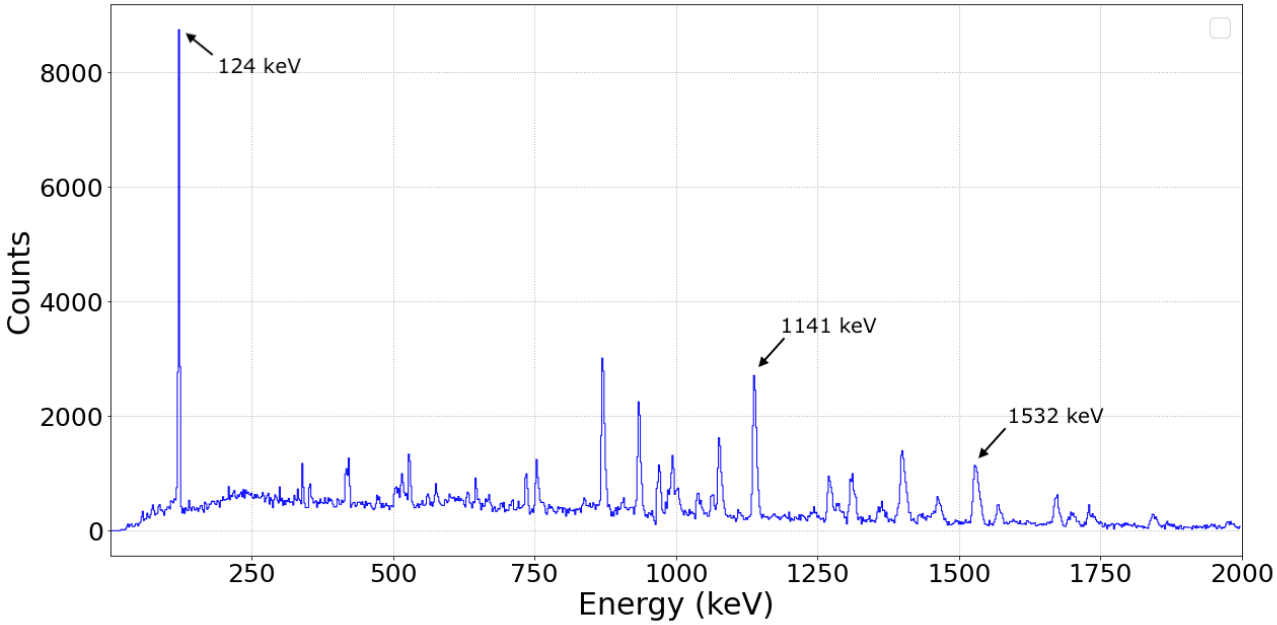

Figure 5.5: The cleaned ^{61}Zn spectrum with γ rays from a few known transitions marked.

3.2 $A = 62$ Separation

After processing the full experimental statistics, there are sufficient statistics from ^{62}Ga transitions to investigate the Z separation in $A = 62$ nuclei. This is done by repeating the procedure described in Section 3.1. The peaks selected for performing the projections of the recoil-γ matrix were: 954 keV from ^{62}Zn and 376 keV from ^{62}Ga. The difference in the abundance of ^{62}Zn nuclei and ^{62}Ga can be easily noticed from the intensities in Figure 5.6.

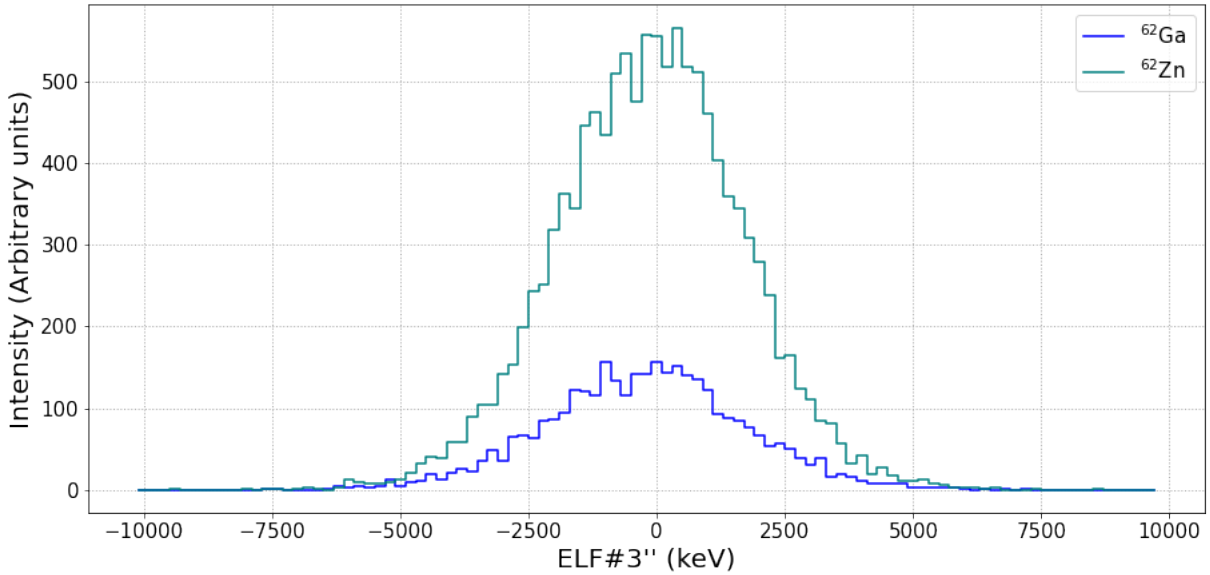

Figure 5.6: Figure showing the IC spectrum for ^{62}Zn (green) and ^{62}Ga (blue) after the second iteration of straightening ELF #3.

The centroid position of the 376 keV peak from ^{62}Ga is not so easily distinguished due to contributions from background (Compton edge). In order to improve this, the background counts were subtracted to highlight the 376 keV peak. This was done by gating on the left and right regions of the peak, projecting those spectra onto the y-axis of the recoil-γ spectrum, and subtracting them from the main IC spectrum of the 376 keV peak. A comparison of the three spectra is seen in Figure 5.7. A slight rise in the right side of the red spectrum may indicate that subtracting it may slightly improve the Z resolution. As seen in the figure, even with attempting to reduce the background, the Z separation is still not sufficient to distinguish $A = 62$ nuclei. This indicated that the ELFs and "straightening" functions may need to be modified for each specific A number.

From Figure 5.7 it is clear that the Z separation is in fact significantly lower in $A = 62$ nuclei compared to $A = 61$ nuclei. As mentioned in Section 5.2, one would expect to see a similar separation in both cases. It may be insightful to further investigate the mass-dependence of the "straightening" function described in Section 5.3 in relation to specifically $A = 62$.

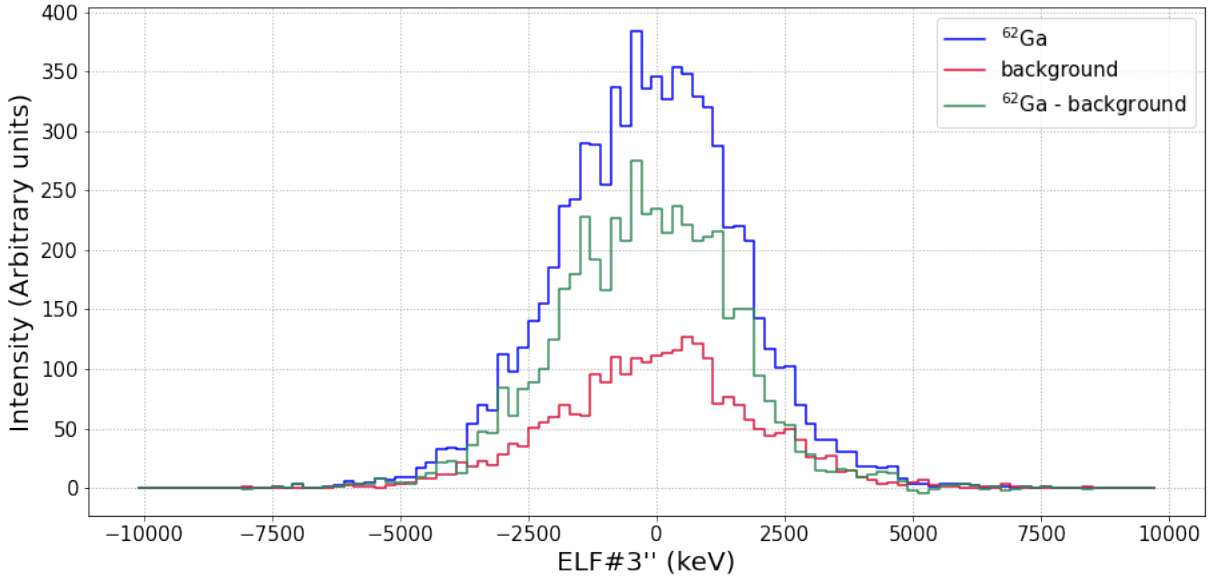

Figure 5.7: The blue spectrum is the IC spectrum of the ^{62}Ga 376 keV peak. The background spectrum (red) is an addition of the IC spectrum from left and right regions around the ^{62}Ga peak. The green spectrum is obtained by subtracting the IC background spectrum from the ^{62}Ga spectrum.

4 Investigating Tentative ^{62}Ge Transitions

Despite lower than expected neutron statistics, it is still of interest to investigate the γ-γ coincidence matrix with the requirements of an anti+coincidence with charged particle and at least one neutron detected. Such coincidence matrices make it possible to gate on a speculated transition ^{62}Ge and see a coincidence spectrum in the projection. By gating on the tentative 964 keV $2^+ \rightarrow 0^+$ ground state transition suggested in Ref. [9], it may be possible to observe an indication of a peak corresponding to tentative 1321 keV $4^+ \rightarrow 2^+$ transition in the projected γ-ray spectrum. The vice-versa can be done to observe the potential 964 keV peak by coincidence gating on the 1321 keV peak. However, due to the low neutron counts, it was not possible to clearly identify any candidates for ^{62}Ge transitions. The γ-γ coincidence matrix gated by $A = 62$ was also investigated. When this was done with the statistics from the full experiment, it was noticed that the overall statistics were also lower than expected from extrapolating from the numbers derived for the subset used for optimizing the analysis procedures. Because of this, as well as the difference in degree of separation of $A = 62$ and $A = 61$ nuclei observed in Sections 3.1 and 3.2, no conclusive evidence to confirm either of the two tentative transitions in ^{62}Ge can be put forward based on the present work.

Chapter 6

Conclusions and Outlook

The 2020 experimental campaign at ANL had one of the most complex and sophisticated setups featuring GAMMASPHERE ever operated. In addition, the experiment was performed during the ongoing corona-virus pandemic, which heavily restricted possibilities of travel. Because of this, the local team at ANL was compelled to assemble the entire setup with limited international assistance on site. Furthermore, during beam time, shifts could only be attended remotely from Lund.

In this thesis work and analysis of the present dataset, an attempt was made to confirm experimental evidence for previously tentative γ-ray transitions assigned to the exotic nucleus ^{62}Ge. However, amid performing the analysis, it was discovered that only 1/8 of the anticipated neutron statistics were available for analysis within the current time frame. This loss in neutron statistics is possibly due to a combination of hardware and software related issues as only 1/4 of the total neutrons were recorded, out of which roughly half were not correlated to any γ rays. Due to this unforeseen complication, it was not possible to select the $^{64}\text{Ge}^* \rightarrow {}^{62}\text{Ge} + 2n$ channel as originally planned. A further investigation into whether some of these neutron events are recoverable will be done by the co-supervisor of this thesis.

Another attempt to select the ^{62}Ge nuclei was made using γ rays measured in coincidence with the detector system in the focal plane of the FMA. In order to confirm the existence of the γ ray transition from the $2^+ \rightarrow 0^+$ state in ^{62}Ge, some additional steps were taken. Firstly, one needs to produce γ-ray spectra for $A = 62$ from the recoil-γ matrix by gating on different intervals of energy losses. However, these spectra will contain γ rays from mainly ^{62}Zn and ^{62}Ga. In order to clean the ^{62}Zn and ^{62}Ga spectra, the γ rays belonging to ^{62}Zn need to be multiplied with a coefficient to match its intensity in the ^{62}Ga spectrum and then subtracted from it. By adjusting the coefficients once again and shifting the ^{62}Zn spectrum, a clean ^{62}Ga spectrum can be produced. The remaining spectra should contain all of the ^{62}Zn and ^{62}Ga peaks, as well as tentative ^{62}Ge peaks.

However, it was found that at the present stage of the analysis, the Z separation for $A = 62$ nuclei was not adequate enough to provide any conclusive evidence about excited states in ^{62}Ge. An investigation into loss of focal plane statistics must also be made along the full experiment. A more thorough exploration of different energy loss functions will hopefully

improve the Z separation further for all $A = 60, 61, 62$ nuclei, however this is beyond the scope of this thesis work.

To conclude, in order to confirm the existence of the γ-ray transitions of ^{62}Ge proposed in [9], more investigation and time has to be put into the present dataset. Finally, comparisons with theoretical shell-model calculations are ongoing. Efforts are currently being made by colleagues from the Division of Mathematical Physics at Lund University to calculate excited states in ^{62}Ge and ^{62}Zn.

A Appendix

Table 6.1: Tablulated values of all the relevant parameters of the efficiency curve fit, for each of the four rings in GAMMASPHERE and their total sum. Details of how they were calculated can be found in Section 2.3.

Ring	Parameter	Value
Total	A	5.5367250
	B	3.3442285
	C	0.0000000
	D	5.5744610
	E	-0.54811847
	F	0.0000000
	G	6.5417762
Ring 1	A	3.5950081
	B	2.7102351
	C	0.0000000
	D	3.8001428
	E	-0.55293989
	F	0.0000000
	G	5.8996391
Ring 2	A	4.0446987
	B	3.0550566
	C	-0.97739142
	D	4.1192164
	E	0.55821174
	F	0.0000000
	G	8.0000000
Ring 3	A	4.1031723
	B	3.1898479
	C	0.0000000
	D	4.3037353
	E	-0.5366888
	F	0.0000000
	G	6.865755
Ring 4	A	4.3326926
	B	2.6733286
	C	0.0000000
	D	4.4491444
	E	-0.54971963
	F	0.0000000
	G	7.2820687

Bibliography

[1] Argonne National Laboratory Official Website. `https://www.anl.gov/`. Accessed December 10 2021.

[2] D. Rudolph et al. Particle and γ-Ray Coincidence Spectroscopy of ^{57}Cu. ANL Proposal.

[3] D.G. Sarantites et al. "The Microball" Design, instrumentation and response characteristics of a 4π-multidetector exit channel-selection device for spectroscopic and reaction mechanism studies with Gammasphere. *Nuclear Instruments and Methods in Physics Research A*, 381:418–432, 1996.

[4] I-Yang Lee. The GAMMASPHERE. *Nuclear Physics A*, 520:641c–655c, 1990.

[5] D. G. Sarantites et al. "Neutron Shell": a high efficiency array of neutron detectors for γ-ray spectroscopic studies with Gammasphere. *Nuclear Instruments and Methods in Physics Research A*, 530:473–492, 2004.

[6] Cary N. Davids and James D. Larson. The Argonne Fragment Mass Analyzer. *Nuclear Instruments and Methods in Physics Research B*, 40-41:1224–1228, 1989.

[7] F.G. Kondev et al. The NUBASE2020 evaluation of nuclear physics properties. *Chinese Physics C*, 45, 2021.

[8] Emma Johansson. *The Quest of Excited States in ^{62}Ge.* MSc. Thesis, 2004. Lund University.

[9] D. Rudolph et al. Exotic Decay Modes in Rotating Nuclei. *Nuclear Physics A*, 752:241c–250c, 2005.

[10] L. Nichols et al. Nuclear Data Sheets for A=62. *Nuclear Data Sheets*, 113, 4 2012.

[11] A. Petrovici. Isospin-symmetry breaking and shape coexistence in A$\approx$70 analogs. *Journal of Physics: Conference Series*, 724, 2016.

[12] H. Schatz et al. End Point of the rp Process on Accreting Neutron Stars. *Phys. Rev. Lett.*, 86(16):3471–3472, 2001.

[13] Michael F. L. Annunziata. *Handbook of Radioactivity Analysis.* Elsevier, third edition, 2012.

[14] Principle of Operation of HPGe Detectors. https://www.nuclear-power.com/nuclear-engineering/radiation-detection/semiconductor-detectors/high-purity-germanium-detectors-hpge/principle-of-operation-of-hpge-detectors/. Edited in 2021, Accessed on September 10, 2021.

[15] E. K. Johansson et al. Isobaric Analog States in Mass A = 62, 61 Nuclides: Mirror Symmetry and Proton Decay in the Upper *fp* Shell. ORNL Proposal, Submission and follow-up of RIB096.

[16] U. Forsberg. Proton-γ Spectroscopy of 65Ar: Isospin Symmetry at the Limits of Nuclear Binding. 2020. ANL Proposal.

[17] C. Fahlander et al. Excited states in ^{103}Sn : Neutron single-particle energies with respect to ^{100}Sn. *Phys. Rev. C*, 63:021307, Jan 2001.

[18] Yuliia Hrabar. Private Communication.

[19] Designing GAMMASPHERE. http://nucalf.physics.fsu.edu/~riley/gamma/gamma3.html.

[20] Pavel Golubev. Private Communication.

[21] Neutron Shell Official Homepage. http://www.chemistry.wustl.edu/~dgs/NeutronShell/NeutronShell.html. Edited on May 9 2004, Accessed on September 10 2021.

[22] L-L. Andersson. *In Quest of Excited States in* ^{61}*Ga*. MSc. Thesis, 2004. Lund University.

[23] Aurora Homepage, Lund University. https://www.lunarc.lu.se/resources/hardware/aurora/. Edited on November 28, 2019, Accessed on September 10, 2021.

[24] LUNARC Homepage, Lund University. https://www.lunarc.lu.se. Accessed on September 10, 2021.

[25] GEBMerge and GEBSort Analysis Codes. https://wiki.anl.gov/gsdaq/Receivers/GEBMerge/GEBsort. Edited on July 11, 2020, Accessed on September 3, 2021.

[26] ROOT Data Analysis Framework Official Website. https://root.cern. Edited 2021, Accessed on September 10, 2021.

[27] CERN Official Website. https://home.cern. Edited in 2021, Accessed on September 10, 2021.

[28] J. Mayer. HDTV: Nuclear Spectroscopy Analysis Tool. University of Cologne, Unpublished.

[29] D. C. Radford. Software or interactive graphical analysis of HPGe coincidence. NIM A 361 297-305, 1995.

[30] Linus Persson. *Digitised charged-particle discrimination in CsI detector signals.* BSc. Thesis, 2022. Lund University.